MODELING OF AMMONIA SYNTHESIS IN A WALL-COATED MEMBRANE MICROCHANNEL REACTOR

by

Emre Küçük

B.S., Chemical Engineering, Boğaziçi University, 2021

Submitted to the Institute for Graduate Studies in
Science and Engineering in partial fulfillment of
the requirements for the degree of
Master of Science

Graduate Program in Chemical Engineering

Boğaziçi University

2023

MODELING OF AMMONIA SYNTHESIS IN A WALL-COATED MEMBRANE MICROCHANNEL REACTOR

DATE OF APPROVAL: 11.07.2023

ACKNOWLEDGEMENTS

I want to thank those who have helped me get through a tough and delicate process of preparing this study. Prof. Ahmet Kerim Avci, whom I will have known for 3 years in two months, has been the kindest and the most supportive teacher and mentor in my educational life. His contributions to my educational and daily life are beyond I can fathom here. I would like to thank him for having been the main guide in creating this work.

I would like to also thank Hayrettin Hasan Koybasi, who at the beginning of my study was amongst the members of the laboratory of Prof. Avci. He has been always kind and supportive as well. He is now a research and teaching assistant at the university of Delaware. Even in his busiest times, he never hesitated to deal with the technical difficulties I came across in preparing this study. I wish the best for him in his new era of his life.

I want to also thank Mert Can Ince, who is the other M. Sc. student in the laboratory of Prof. Avci. He is also beginning a new career abroad. I wish the best for him in his future.

I would like to also thank the other members of the laboratory of Prof. Avci; Mert Ozden, Necdet Semih Altinsoy, and Orhun Harmancilar.

My biggest thanks go to my family. I would like to thank them for always supporting me. I would like to thank them for always being by my side when I was exhausted. I would like to thank them for everything.

I was funded by TUBITAK while preparing this project. I thank them for their support. The project codes are 118M518 and 120M412.

ABSTRACT

MODELING OF AMMONIA SYNTHESIS IN A WALL-COATED MEMBRANE MICROCHANNEL REACTOR

Ammonia (NH_3) synthesis is modeled in a micro–structured membrane reactor (MR) comprising reaction, cooling and NH_3 separation functions in the same volume. The proposed MR involves permeate and reaction channels segregated by layers of zirconia supported $ZnCl_2$ immobilized molten–salt (IMS) membrane selective to NH_3 transport. While H_2+N_2 is fed to reaction channels washcoated with an iron–based catalyst, permeate channels host N_2 as the sweep gas which also regulates reaction temperature. The *in–situ* cooled MR is modeled by considering mass, momentum and energy conservation in the fluid phases of the reaction and permeate channels, reaction in the catalyst layer and NH_3 transport across the membrane, whose thermal stability limit of 623 K is set as the maximum reactor temperature. Upon N_2 sweep dosing equal to 50 × the molar H_2+N_2 input at $H_2/N_2=3$, 613 K, 50 bar and 1.5×10^3 m^3 kg_{cat}^{-1} s^{-1}, MR can deliver ~47% N_2 conversion which exceeds 40 and 13.5% of the pertinent thermodynamic barrier and the membraneless case, respectively. Despite the exothermic heat release, co–current partitioning of the streams ensures operability below 623 K. Increasing space velocity and H_2/N_2 ratio, and decreasing inlet temperature and pressure inhibit reactor performance. Using molar sweep–to–reactive mixture ratios <50 is penalized by the violation of the specified maximum temperature.

ÖZET

MEMBRAN ENTEGRELİ KAPLANMIŞ MİKROREAKTÖRDE AMONYAK SENTEZİNİN MODELLENMESİ

Amonyak (NH_3) sentezi; reaksiyon, soğutma, ve NH_3 ayırma fonksiyonlarını aynı hacimde içeren mikro yapılı membran reaktörü (MR) içinde modellenmiştir. Önerilen membrane reaktörü, NH_3 transferine karşı seçici, zirkonya ile desteklenmiş, $ZnCl_2$ bazlı, sabitlenmiş eriyik tuz (IMS) membran ile ayrılan reaksiyon ve süpürme kanallarını içermektedir. H_2 ve N_2, demir bazlı katalizörle kaplanmış reaksiyon kanallarına beslenirken, süpürücü gaz olarak N_2 kullanan süpürücü kanallar aynı zamanda reaksiyon sıcaklığını da düzenlemektedir. Aynı yerde soğutulan membran reaktör; kütle, momentum, enerji korunumu, katalizör tabakasındaki reaksiyon, ve sıcaklık stabilite limiti 623 K olan membran içinde gerçekleşen amonyak kütle transferi olaylarını hesaba katarak modellenmiştir. N_2 süpürücü gazın molar akış hızının, $H_2/N_2=3$ iken H_2+N_2 molar akış hızından 50 kat fazla olduğu durumda, 613 K, 50 bar, ve 1.5×10^3 m^3 kg_{cat}^{-1} s^{-1} şartlarında, membran reaktörü %47 N_2 dönüşümü sağlayarak sırasıyla %40 olan ilgili termodinamik N_2 dönüşüm bariyeri ve %13.5 olan membransız N_2 dönüşümünü aşmıştır. Ekzotermik ısı yayılımına rağmen, eşyönlü olarak verilen akımlar 623 K altında operasyonu garanti etmiştir. Akış hızını ve H_2/N_2 oranını artırmak, giriş sıcaklığını ve basıncı düşürmek reaktör performansını düşürmektedir. Molar olarak 50'den aşağı seviyede süpürücü/reaktif karışım oranı kullanmak maksimum sıcaklık sınırının aşılmasına neden olmaktadır.

TABLE OF CONTENTS

LIST OF FIGURES

LIST OF TABLES

LIST OF SYMBOLS

$c_{p,i}$	Heat capacity of species i, J kg^{-1} K^{-1}
$c_{p,m}$	Heat capacity of gas mixture, J kg^{-1} K^{-1}
D_{ij}	Binary diffusion coefficient, m^{2} s^{-1}
$D_{K,i}$	Knudsen diffusivity of species i, m^{2} s^{-1}
d_{part}	Particle diameter, m
d_{pore}	Average pore diameter, m
J_i	Mass flux of species i through membrane, mol m^{-2} s^{-1}
K_{eq}	Reaction equilibrium constant, bar^{-2}
K_a, K_b	Parameters of the rate law used in this report, K_a: bar$^{-0.5}$, K_b: bar$^{0.5}$
k_{cat}	Thermal conductivity of catalyst layer, W m^{-1} K^{-1}
$k_{eff,m}$	Effective thermal conductivity of gas mixture in the washcoat layer, W m^{-1} K^{-1}
k_i	Thermal conductivity of species i, W m^{-1} K^{-1}
k_m	Thermal conductivity of gas mixture, W m^{-1} K^{-1}
k_w	Thermal conductivity of the solid wall, W m^{-1} K^{-1}
M_i	Molecular weight of species i, kg mol^{-1}
M_m	Average molecular weight of gas mixture, kg mol^{-1}
n_i	Number of moles of species i, mol
N_g	Number of gas-phase species, –
p	Total pressure (equal to p_{in}^{R}), bar
p_i	Partial pressure of species i in the reaction channel, bar
p_{in}^{R}	Pressure at the inlet of reaction channel, bar
R	Gas constant (=8.314 J mol^{-1} K^{-1})
r	Rate of reaction, kmol m^{-3} s^{-1}
T	Temperature, K
$\vec{\boldsymbol{v}}$	Velocity vector, m s^{-1}
y_i	Mole fraction of species i, –

ΔH^{o}	Heat of reaction at standard conditions, kJ mol^{-1}
ΔH	Heat of reaction, kJ mol^{-1}
$\varepsilon_{\mathrm{cat}}$	Porosity of the washcoat layer, –
ϕ_{ij}	Dimensionless parameter for the mixture of *i* and *j*, –
μ_i	Viscosity of species *i*, kg m^{-1} s^{-1}
μ_m	Average gas mixture viscosity, kg m^{-1} s^{-1}
ρ_m	Density of gas mixture, kg m^{-3}
τ_{cat}	Catalyst tortuosity, –
ξ_i	Extent of reaction *i*, mol
$\left(\sum \upsilon\right)_i$	Sum of the atomic diffusion volumes for species *i*, –

LIST OF ACRONYMS/ABBREVIATIONS

cat	Catalyst
CP	Catalyst phase
FP	Fluid phase
in	Inlet
m	Mixture
M-	Membraneless case
ML	Membrane layer
P	Permeate channel
R	Reaction channel
SV	Space velocity
TD	Thermodynamic limit

1. INTRODUCTION

The world population has been growing for years. In fact, the 8 billion benchmark was achieved near the end of 2022. The growth rate is so intense that the number of population is expected to increase and eventually peak at about 10 billion [1]. Consequently, more and more energy and supply demand are imposed upon the world. As industries thrive to meet the demands of the public utilizing this energy, global pollution and greenhouse emissions rapidly increases as well. The world also tries to adapt better techniques to harness cleaner sources. In 2021, EU obtained more than 22% of its energy out of renewable sources, with their aim pointed at 95% by year 2050 [2].

Another important achievement came from the U.S. in 2022 as the electricity generated by means of renewable energy exceeded the electricity produced by coal, for the first time in their history [3].

Although the transition to clean sources increases every day, it is still not enough to cover a substantial portion of the world energy demand. Nonetheless, the share of renewable sources of energy in the world energy consumption is increasing steadily [4].

Industries that create outputs of enormous amounts should try to adapt better and more efficient techniques to yield more environmentally-friendly processes. Today, ammonia, a material of immense importance is produced dominantly by Haber-Bosch process. The process is so important that it was associated with the “modernity” of the current civilization [5].

The well-known Haber-Bosch process has been used extensively for years. However, the process requires extensive conditions due to thermodynamic limitations. The process merges hydrogen with nitrogen to produce ammonia, and it was the first industrial process that utilized high pressure in order to induce a chemical reaction [6].

The importance of ammonia must be mentioned. It is denoted as the second chemical substance in global production. It can be used in all phases, although the gas and liquid phase use are more dominant over the solid phase. Its storing is easier than hydrogen, requiring lower pressure to be stored. It might be utilized as a refrigerant fluid in some cyclic applications. Its transportation is also relatively easy with low maintenance requirements. There is no carbon atom in ammonia structure, making it a clean and sustainable hydrogen carrier [7].

According to a 2017 study, nitrogen captured from atmosphere in amount of more than 100 million metric tons is utilized to produce ammonia via Haber-Bosch process [8]. A 2015 study gave even stricter number, indicating that the amount is more than 130 million metric tons each year and also the process itself consumes about 1-2% of world's energy consumption while assuming the role of sustaining 40% of the world population [9].

Indeed, according to a 2008 study, thanks to Haber-Bosch process, in 1908, number of humans provided per hectare of arable land was only 1.9. This number was anticipated to be 4.3 in 2008. The study also drives home the fact that nitrogen fertilizers were responsible for supporting about 27% of the population of the past century [10]. The production trend follows the same steadily-increasing trend for years worldwide [11].

The reactants for the Haber-Bosch process also require complicated processes. Steam reforming is the process implemented to deliver the hydrogen needed for ammonia synthesis. The nitrogen comes from a secondary reforming operation of air. The upstream operations include some reactions and separation operations to finally deliver the pure hydrogen and nitrogen mixture as feed to the ammonia synthesis reactor[12]. Moreover, the feed must be pressurized to intense levels, up to 100-300 bar and also heated to 300-550 ^{o}C [13].

The Haber-Bosch process has a huge capacity, with the 'low-capacity' plants being reported at 30000 tons annually [14]. A more efficient process that is capable of producing ammonia at lower scale would be beneficial. The demand on low capacity production comes from the increasing need for on-site ammonia production that cannot be realized profitably with the conventional Haber-Bosch process.

Here, we present a wall-coated catalytic membrane microchannel reactor that can help downscaling of ammonia synthesis efficiently. The study focuses on the effectiveness of the configuration and also the effects of changing the operating parameters on reactor temperature and nitrogen conversion. The mathematical model is represented and the justification of rate of reaction is done with the discussion of the results.

2. LITERATURE SURVEY

2.1. The Haber-Bosch Process: Fundamentals and Catalysts

90% of ammonia produced worldwide still relies on the Haber-Bosch process, which has undergone no significant change for years [15]. The reaction proceeds as follows when adjusted for one mole of nitrogen, it is represented as

$$N_2 + 3H_2 \rightleftharpoons 2NH_3 \,. \tag{1.1}$$

The standard heat of reaction per one mole of nitrogen is reported as[15]

$$\Delta H_{298} = -92.4 \, \frac{kJ}{mol} \,. \tag{1.2}$$

The reaction is highly exothermic. Due to thermodynamics, single pass conversions are rather low and reported to be around 10-15% at conditions of 400-500 °C and 100-300 bar [16].

The process starts with desulphurization, where natural gas is stripped from the sulfur content to prevent sulfur poisoning of the catalysts involved in the process. Desulphurized natural gas then reacts with steam, giving the products hydrogen, carbon monoxide, carbon dioxide, and methane. Primary reforming is an endothermic reaction, so a furnace provides the necessary heating. Secondary reforming process involves the adding of air, providing the nitrogen content for ammonia production and also the oxygen content that converts the methane that has not been converted in the primary reforming in an exothermic reaction. The heated products are then cooled and forced to undergo two water-gas shift reactions, which reacts the carbon monoxide content in the reactants with steam and yields hydrogen and carbon dioxide as the products. Remaining carbon dioxide is stripped from the contents by absorption and CO/CO_2 cleanup operations. The remaining content is pressurized and fed to the reactor. Finally, a recycle stream is fed to the reactor to convert the unconverted reactants [17].

As the reaction is exothermic, thermodynamics and rate of reaction favor reverse paths for temperature profile. The reaction step therefore includes cooling operation. Internal direct cooling, adiabatic quench cooling, or adiabatic indirect cooling can be applied [18].

Various types of catalyst have been examined so far for Haber-Bosch process. It is not possible to cover all of them here. However, a detailed literature survey was performed. For more detailed information, the reader is advised to refer to the work of Humphreys *et al*. [19] where detailed research was performed on the catalyst studies for Haber-Bosch process.

2.1.1. Iron-based Catalysts

Han *et. al* [20] investigated the effect of Nobium on wustite-based catalyst, abbreviated as WBC, with Nobium acting as a promoter. WBC catalyst contained 80.46 wt% FeO, 12.66 wt% Fe_2O_3 with the rest being other compounds containing Al_2O_3, K_2O, and CaO. Nb-WBC catalyst contained 80.00 wt% FeO, 12.52 wt% Fe_2O_3 with the rest being other compounds containing Al_2O_3, K_2O, and CaO and Nb_2O_5. To produce the catalyst they investigated, they mixed iron powder, purified magnetite, alumina, potassium nitrate, calcium carbonate, and some other promoters in appropriate proportions and melted the mixture via electric resistance furnace at temperatures about as high as 1600 °C. Additional powder acted as a reducing agent to adjust Fe^{2+} / Fe^{3+} ion ratio in WBC. After melting was completed, the melt was poured outside and cooled by water. For WBC catalyst doped with Nb_2O_5, 0.6 wt% of Nb_2O_5 was also included in the promoters. After crushing and screening out operations, the irregular catalysts of sizes between 1.0 mm and 1.4 mm were gathered. It was shown that the catalyst doped with Nb_2O_5 had 25 °C lower reduction temperature than that of WBC and also faster reduction rate. However, the activity of WBC doped with Nb_2O_5 was reported to be a bit lower than that of standard WBC. It was also reported that the fact that WBC doped with Nb_2O_5 had lower reduction rate renders it more advantageous in industrial applications.

Yu *et al.* [21] investigated the effect of rare earth gangue, namely a mixture of lanthana, ceria, neo dymium oxide and praseodymium oxide, as promoter in fused iron catalysts. It was seen that comparable activity could be achieved to that of commercial iron catalysts that include high amount of cobalt. Therefore, it was asserted that a potential to completely replace cobalt in the catalyst existed, which would lead to important cost reductions in the catalysts. Moreover, it was found that the catalysts with low rare earth gangue contents were reduced easily. In this study, three different catalytst were prepared for testing, namely FA400, FA401, and FA402. The rare earth gangue content for preparation was taken from a company in China. Compound compositions of the unreduced catalyst samples were given. For FA400, contents are 69.0 wt% total Fe, 2.4 wt% Al_2O_3, 1.4 wt% CaO, 0.60 wt% K_2O, 0.34 wt% SiO_2, 0.3 wt% MgO. For FA401, contents are 68.0 wt% total Fe, 2.3 wt% Al_2O_3, 1.1 wt% CaO, 0.58 wt% K_2O, 0.33 wt% SiO_2, 0.3 wt% MgO. For FA402, the contents are 68.0 wt% total Fe, 2.4 wt% Al_2O_3, 1.1 wt% CaO, 0.58 wt% K_2O, 0.39 wt% SiO_2, 0.4 wt% MgO, and 0.5 wt% Co_3O_4.

Pilecka *et al.* [22] prepared iron and Co-Fe catalyst that were deposited on carbon and examined for ammonia synthesis at 90 bar and H_2:N_2 ratio of 3. Commercial activated carbon was treated at 1900 °C and graphitized carbon obtained from that operation was implemented as support for the 10 wt% active metals, with barium and potassium acting as promoters. There was data for two types of carbon-based Co-Fe catalysts. The first one was carbon-based Co-Fe catalyst with potassium promoter and the second one was carbon-based Co-Fe catalyst with barium promoter. Several different compositions were studied. The catalysts studied included Fe_{10}/C, K-Fe_{10}/C, K-$Co_{0.5}$-$Fe_{9.5}/C$, K-$Co_{1.0}$-$Fe_{9.0}/C$, K-$Co_{2.0}$-$Fe_{8.0}/C$, Ba-Fe_{10}/C, Ba-$Co_{0.5}$-$Fe_{9.5}/C$, Ba-$Co_{1.0}$-$Fe_{9.0}/C$, Ba-$Co_{2.0}$-$Fe_{8.0}/C$. The subscripts denoted the wt% of the contents on carbon. It was observed that for Co-Fe catalysts promoted with potassium, as wt% of Co increased and wt% of Fe decreased, activity increased. However, for Co-Fe catalysts promoted with barium, as wt% of Co increased and wt% of Fe decreased, activity decreased as well. Moreover, according to the data, potassium promoted samples were more active. The samples were 500 mg with the flow rate adjusted at 70 dm^3 (STP)/h . Data for KM1 produced by Topsoe was also included for comparison. The reader is referred to the table presented in the study.

Jafari *et al.* [23] prepared and examined wustite-based iron catalysts that are triply promoted and they compared it to magnetite catalyst that they prepared similarly. The raw materials used in the preparation was denoted magnetite, iron powder, aluminum oxide, calcium carbonate, and potassium carbonate with high purity. The promoters in the samples for comparison were denoted to be the same and also less than 10wt%. The contents of the materials on the surface of the wustite catalysts were given as 2.4 atomic % Al, 0.31 atomic

% K, 1.00 atomic % Ca, 30.62 atomic % Fe, and 65.7 atomic %O with their deviation percents denoted as well. For magnetite catalysts, the contents on the surface were given as 3.3 atomic % Al, 0.23 atomic % K, 0.54 atomic % Ca, 30.24 atomic % Fe, and 65.7 atomic %O with deviation percents reported. The reader is referred to the table for full representation. It was observed at the end that wustite-based iron catalyst displayed better performance. Moreover, reduction temperature was lower and activation was quicker as well. Activity was also found to be higher, accompanied by reasonable mechanical strength and thermostability. Due to these results, it was asserted that wustite-based iron catalysts could be an alternative to magnetite-based catalysts in industry with advantages such as lower energy consumption and lower CO_2 emissions in the ammonia production plants.

Taylor *et al.* [24] examined various iron-cobalt and iron-nickel catalysts after reducing them at 853 K for 18 hours. They also computed the metal surface areas of the catalyst by carbon monoxide absorption. Aqueous solutions of mixed metal nitrates were co-precipitated by ammonium bicarbonate solution addition. Aluminum nitrate addition before precipitation was adjusted such that catalyst contained about 3 wt% of alumina which served the role of structural stabilizer also prevented sintering during the reaction occurs, thereby preventing the loss of metal area. It was reported that the amount of sulphure, halogen, or alkali was less than 0.02 wt% in the catalysts. Several catalysts, reported as Fe(20)Co(80), Fe(40)Co(60), Fe(60)Co(40), Fe(80)Co(20), Fe(90)Co(10), Fe(95)Co(5), Fe(95)Ni(5), Fe(90)Ni(10), Fe(85)Ni(15), Fe(80)Ni(20), Fe(60)Ni(40), and Fe(30)Ni(70) were examined. It was found that Fe(95)Co(5) had the highest activity. For iron rich nickel catalysts, the maximum activity was obtained with the catalyst Fe(90)Ni(10). Possible explanations included there was a possibility that greater surface area occurred in certain parts of the catalyst.

Baiker *et al.* [25] examined the catalyst obtained by the preparation of in situ activated amorphous $Fe_{91}Zr_9$. When the conditions of 9 bar, 690 K, and stoichiometric feed were exposed on $Fe_{91}Zr_9$, about 500 hours were needed to obtain strongly active and stable catalyst. Throughout this timespan, amorphous $Fe_{91}Zr_9$ that was inactive was undergoing chemical changes. Moreover, it was asserted that the time needed to obtain highly active catalyst could be reduced by applications of oxygen pulses to the precursor at the reaction temperature. When compared to the polycrystalline iron, the activity of such catalysts was found to be higher. Reaction rates as high as about 20 nmol s^{-1} g^{-1} , or about 72 μmol h^{-1} g^{-1} was obtained after 500 hours timespan needed to fully activate the catalyst at 9 bar, 690 K, with stoichiometric feed fed at a rate of 40 mL (STP)/min.

Wang *et al.* [26] examined the effect of LiH on Fe. Neat polycrystalline Fe had negligible activity compared to Fe-xLiH catalysts. Fe-LiH, Fe-3LiH, Fe-5LiH, and Fe-10LiH catalyst were compared. They showed comparable performances in terms of ammonia synthesis rates, with Fe-5LiH taking the edge by a slight margin. Figure 1 represented in this study showed ammonia synthesis rates being observed also from the perspective of amount of Fe present in the catalysts. Different results were obtained. The significance of contact and interface between Fe and LiH was pointed out as a potential reason.

Kitano *et al.* [27] investigated a novel catalyst, namely perovskite oxynitride-hydride, $Ba\text{-}CeO_{3-x}N_yH_z$ that was synthesized by the reaction of $Ba(NH_2)_2$ and CeO_2 at temperatures between 300-600 °C. The mentioned catalyst was asserted to be an efficient catalyst for ammonia synthesis through a number of specified mechanisms. It was also mentioned that rate-redetermining step was shifted in the catalyst. Different catalysts with Fe and Co contents were given. $Fe/BaCeO_{3-x}N_yH_z$ was reported to have nearly 7 mmol g^{-1} h^{-1} ammonia synthesis rate at 400 °C at 0.9 MPa.

Murakami *et al.* [28] pointed out that although Ru-supported catalysts had higher turn-over frequency (abbreviated as TOF) than Fe-supported or Ni-supported catalysts, they found out that the reverse turned out to be true at 373 K when electric field was applied. Their calculations through density functional theory (DFT) displayed that N_2 dissociation by associative mechanism was the crucial factor in the electric field. Figure 1 in the study displayed the data for ammonia synthesis rates for 7 wt% Metal/CeO_2 catalysts (Metals are Ru, Fe, Co, Ni, Pd, Pt) with and without the application of electric field at 723 K, 0.1 MPa. The electric field intensity was 6 mA. For no-electric field application, ammonia synthesis rate was highest by a large margin for 7 wt% Ru/CeO_2, with 7 wt% Fe/CeO_2 being the second. When the electric field was applied, the highest ammonia synthesis rate was obtained in 7 wt% Fe/CeO_2 with 7 wt% Ni/CeO_2 being the second. The third highest value was obtained in 7 wt% Ru/CeO_2. In this study, CeO_2 was chosen to be the catalyst support. Active metals denoted (Ru, Fe, Co, Ni, Pd, Pt) was loaded onto the support by impregnation method.

Fan *et al.* [29] created a new catalyst with the intention to make a more economical and powerful counterpart of industrial Fe-based catalysts, which as they mentioned required sophisticated and energy-requiring processes treatments. They made FeOOH nanosheets with δ-Al_2O_3 supports. They also investigated unsupported FeOOH and K-promoted catalysts. There was no activity for FeOOH catalysts without support, while the activity of δ-Al_2O_3 supported catalysts decreased when amount of Fe increased. It was observed that the activity and metallic Fe particle size were correlated. The synthesis methods of the nanosheets can be found by the previous work of the authors. The rates of ammonia synthesis in Figure 5 clearly indicated that FeOOH/Al_2O_3 (5%Fe) had higher rate than FeOOH/Al_2O_3 (15%Fe) and FeOOH/Al_2O_3 (25%Fe) at all temperatures tested. However, FeOOH-K/Al_2O_3 (25%Fe) showed the best performance in terms of ammonia synthesis rate by a large margin. The test conditions were adjusted such that stoichiometric feed was fed, the pressure was 90 bar, and the temperature was 500 ^oC.

Yan *et al.* [30] proposed a strategy to develop K-promoted Fe/C catalyst with Fe contents more than 50 wt% via Fe-based metal-organic framework (MOF) xerogel pyrolysis. The reaction rates of Fe/C catalyst with K_2O acting as the promoter were given as 12.4 mmol g^{-1} h^{-1} at 350 ^oC and 30.4 mmol g^{-1} h^{-1} at 400 ^oC , which were much higher than that of commercial fused-iron catalysts with rate values given as 3.4 mmol g^{-1} h^{-1} at 350 ^oC and 16.7 mmol g^{-1} h^{-1} at 400 ^oC. The huge improvement was attributed to the fact that potassium promoter affected reactant molecules on Fe surface by changing their binding energies and that the catalyst had obtained a special structure from metal-organic frame precursors. The pressure in the experiment was 3 MPa.

Czekajło *et al.* [31] examined Fe and Fe-Co wustite based catalysts that were promoted with calcium oxides, aluminium oxides, and potassium oxides. Activities were calculated at 10 MPa. Prepared ZBRW-10 catalyst contained 2.18 wt% Al_2O_3, 1.3 wt% CaO, 0.44 wt% K_2O, and 2.01 wt% CoO. Prepared ZBRW-11 catalyst contained 3.36 wt% Al_2O_3, 2.09 wt% CaO, 0.67 wt% K_2O, and 3.62 wt% CoO. ZBRW-10 catalyst displayed the highest activity, with ZBRW-11 being the second in terms of activity. When reduction temperatures were increased to excessive levels, both catalysts suffered activity losses. Therefore, it was asserted that wustite based catalysts respond more to temperature increases compared to industrial magnetite based iron catalysts.

Tang *et al.* [32] investigated ammonia synthesis with oxyhydride $BaTiO_{2.5}H_{0.5}$ over which Ru, Fe, and Co particles were supported. It was found out that the activity of the catalyst with $BaTiO_{2.5}H_{0.5}$ support was much higher than the catalyst with $BaTiO_3$ support. Ammonia synthesis rate measured with Fe/ $BaTiO_{2.35}H_{0.65}$ was 70 times the rate measured with Fe/$BaTiO_3$, rendering its activity higher than conventional Ru/MgO catalyst. For Fe, activation energy and N_2 reaction order were reduced due to hydride presence, with the possible reason being strong electron donation from the oxyhydride.

2.1.2. Nickel-based Catalysts

Ye *et al.* [33] suggested that Ni loaded lanthanum nitride (LaN) can generate ammonia by being highly efficient and stable due to dual-site mechanism. The activity was measured to be 5.543 μmol g^{-1} h^{-1} at 400 °C for Ni/LaN nanoparticles. The values obtained were pointed out as being much higher than traditional conventional nickel and conventional cobalt based catalysts. Ni/LaN nanoparticles performed better in terms of ammonia synthesis rate than Ni/LaN bulk catalyst did.

Kojima *et al.* [34] investigated bimetallic molybdenum nitride catalysts they prepared. The preparation was done by nitriding oxide precursors with ammonia at temperatures as high as 973 K. In kinetic studies, stoichiometric feed of nitrogen and hydrogen was used with flow rate of 60 ml min^{-1} on 0.4 g catalyst at temperatures 588-673 K and pressures of 0.1-3.1 MPa. It was seen that the rate of reaction as pressure increased. The rate at 673 K and 3.1 MPa for Co_3Mo_3N catalyst was measured to be 4.8 mmol h^{-1} g^{-1}. This value was significantly higher than molybdenum bimetallic nitride catalysts with iron or nickel that were prepared similarly to Co_3Mo_3N catalyst. With the addition 2 mol% Cs Co_3Mo_3N catalyst, the ammonia synthesis rate increased to 4.6 mmol h^{-1} g^{-1} at 3.1 MPa. The characteristic that Co_3Mo_3N catalyst was inhibited more by ammonia was prevented by alkali promoter addition.

Bion *et al.* [35] asserted that the catalytic performance of Ni_2Mo_3N samples was strongly affected by the preparation method implemented for ammonia synthesis carried out at ambient pressure. They found that when $NiMoO_4$ precursors were used, a lot of Ni impurity phase occurred, which led to the materials forming from these precursors to be inactive for synthesis of ammonia, while it was possible to implement a modified form of Pechini method by using citrate gels which resulted in highly active Ni_2Mo_3N. By N_2/H_2 pre-treatment, Ni_2Mo_3N could be prepared, which was an advantageous method. Overall, Ni_2Mo_3N prepared by Pechini method was found to be a fit catalyst for ambient pressure ammonia synthesis.

Ye *et al.* [36] asserted a general rule for designing of nitride-based catalysts. In their experiments, they found that Ni/CeN catalyst could achieve an activity of 6.5 mmol g^{-1} h^{-1} at 400 °C and 0.1 MPa, which was far greater than other Co-based and Ni-based catalysts, while being close to the those of Ru-based catalysts. They carried out density functional theory (DFT) calculations and found that nitrogen and hydrogen were activated when the reaction occurred by the nitrogen vacancies in CeN.

Humphreys *et al.* [37] found that catalytic activity of Ni to synthesize ammonia could be significantly increased by proton-conducting oxide $BaZr_{0.1}Ce_{0.7}Y_{0.2}O_{3-\delta}$ (BZCY). An investigation on the optimum operating conditions was carried out and it was found that 250 μmol g^{-1} h^{-1} of catalytic activity could be achieved at 620 °C and 200 mL min^{-1} flow rate with stoichiometric feed of hydrogen and nitrogen. This value was 10 times that of unpromoted Ni catalyst under the same operating conditions. However, the stabilities of both of these catalysts were bad when steam was present. The catalytic activity of Ni catalysts supported on BZCY was also found to be 72 times greater than the catalytic activity of Ni catalysts supported $MgO\text{-}CeO_2$, which was a non-proton conductor. They suspected that the great enhancements in catalytic activities stemmed from the property of the supports that they were proton conducting. Due to these observations, it was asserted that Ru and Fe catalysts which are highly active catalysts used for ammonia synthesis would enhance the activity of these catalysts at low temperatures if they were modified by proton conducting supports.

2.1.3. Ruthenium-based Catalysts

Narasimharao *et al.* [38] examined Ru catalysts supported by carbon covered hydrotalcite (CCHT) which were promoted either singly or doubly (by Cs or Ba) that were prepared by either impregnation (IMP) and polyol reduction (PR) methods by implementing ethylene glycol as a solvent. Catalytic performances were measured at atmospheric pressure and temperatures ranging from 523 K to 698 K. In terms of % ammonia (volume/volume) formation, the performances of the catalysts were ordered as BaRuCCHT-IMP < BaRuCCHT-PR < CsBaRuCCHT-IMP < CsRuCCHT-IMP < CsRuCCHT-PR < CsBaRuCCHT-PR. They implemented methods of X-ray diffraction, TEM, H_2-TPR, carbon monoxide chemisorption, TPD, and nitrogen adsorption to obtain the reasons why CsBaRuCCHT-PR performed better than its rivals in terms of catalytic activity and also to obtain physical and chemical properties of all the catalysts. It was asserted by TEM and carbon monoxide chemisorption studies that that low particle size, high surface area, high active surface metal (Ru) area, and the strong interactions between Ru and CCHT could be the reasons why CsBaRuCCHT-PR had the highest catalytic activity.

Wildfire *et al.* [39] implemented microwave with constant frequency of 2.45 GHz to produce ammonia with Ru/MgO catalyst at atmospheric pressure and 320 °C. The amount of Ru on MgO was changing between 4 wt% and 10 wt%. It was found that when the Ru loading was the highest at 10 wt%, the catalysts had the highest activity, stability, and efficiency as well. The interaction between the metal and the support was important not only in the catalytic properties but also in modifying the bond between the microwave and the catalyst, which influence the rate at which ammonia was produced. The sintering effect owing to the decreased microwave energy that was needed to keep the reaction temperature at the desired level was greatly reduced by Ru dispersing better when the loading was higher. Two possible additional influences due to the presence of microwave were presented as enhanced electron movement and electric fields that might have formed between the catalyst metal sites. It was also found that the microwave reactor had 11 min of catalyst on/off recovery, which was higher than conventional Haber Bosch process.

Hattori *et al.* [40] pointed out to the fact that there was a lack of efficient catalyst to produce ammonia at low temperatures such as 50 °C, which halted the movement toward lower carbon dioxide emissions. They presented CaFH, which was a solid solution formed at low temperatures from materials CaF_2 and CaH_2. This catalyst had an activation energy as low as 20 kJ/mol and was able to synthesize ammonia at 50 °C. The activation energy they found was said to be less than half of that of conventional catalysts. The possible explanations due to high catalytic performance were explained as weak ionic bonds formed between H^- and Ca^{2+} ions and hydrogen atom releasing easily from H^- sites. In the experiment they conducted on catalytic performance, carried out at silica-glass fixed bed reactor loaded with 0.1 of catalysts fed with stoichiometric mixture of nitrogen and hydrogen having a weight hourly space velocity of 36000 mL $gcat^{-1}$ h^{-1} under atmospheric pressure, Ru/CaFH loaded with 12 wt% Ru displayed much higher ammonia formation rates than those of Ru/BaO-BaH_2 loaded with 10 wt%, Ru/CaH_2 loaded with 10 wt%, Cs-Ru/MgO loaded with 10 wt%, and commercial Fe catalysts, with values reported as 50, 75, 120, and 190 μmol g^{-1} h^{-1} at 50 °C, 75 °C, 100 °C, and 125 °C, respectively.

Hattori *et al.* [41] also investigated the effectiveness of using a mixture of BaO ad CaH_2 powders with nanoparticles of ruthenium, which have relatively small activation energy of 41 kJ mol^{-1}, to synthesize ammonia at low temperatures. The good performance of the catalyst was attributed to the transformation of BaO caused by the reaction of BaO with CaH_2. The strong catalytic performance stemmed from BaH_2 in the transformed BaO, which was a stable and strong electron donator. This material enabled a reversible reaction in which hydrogen was stored and released, while also enhancing electron donation phenomenon to Ruthenium. In an experiment conducted at 0.1 MPa and 340 °C with stoichiometric feed of hydrogen and nitrogen fed at 60 mL min^{-1} to 0.1 g of Ru(10 wt%) / BaO-CaH_2 catalyst, ammonia formation rate of 10.5 mmol h^{-1} g^{-1} was achieved. Ru (10 wt%) / CaH_2 was able to achieve 7.4 mmol h^{-1} g^{-1}, while the value obtained for Ru(10 wt%) / Ba-$Ca(NH_2)_2$ was the highest at 12.4 mmol h^{-1} g^{-1}.

Kitano *et al.* [42] asserted that a chlorine-tolerant Ruthenium based catalyst made of $12CaO.7Al_2O_3$ with sub nanometer-sized cages was effective against poisoning due to chlorine ions, which conventional Ruthenium based catalysts suffered due to electron-withdrawing effect of chlorine ions. They indicated that even a small amount of chlorine ion presence on the catalyst surface caused a huge drop in the activity of Ruthenium based catalysts in general. However, Ru/C12A7 was highly tolerant and did not suffer low activity even when the amount of chlorine was much higher than it was for conventional Ruthenium based catalysts. It was asserted that C12A7 sub nanometer-sized cages that had positive charges were able to imprison the chlorine ions instead of OH^- ions. They prepared C12A7 material via hydrothermal method (HT-C12A7) and found that it also acted as a good support. They proposed that C12A7 could be used as a catalyst support for metals Pt, Pd, Cu, and Ni.

Qiu *et al.* [43] was able to achieve higher performance in terms of activity than traditional Ru catalyst (Cs-Ru /MgO) with pure siliceous zeolite-supported Ru SAC (Ru Sas/S-1) at the same conditions. Ba promoter addition led to a catalytic activity of 1389.5 μmol h^{-1} g_{cat}^{-1} achieved at 673 K, which was a value reported to be about 2 order of magnitude higher than the value achieved for unpromoted catalyst. They proposed that the study offered an alternative for the design of high-performance Ruthenium based catalysts.

Li *et al.* [44] prepared CeO_2 supports with $C_{12}H_{29}NO$ (TPAOH), $C_2H_8N_2$ (EDA) and NaOH, all acting as precipitants at hydrothermal conditions. The catalysts were prepared via incipient impregnation. At an experiment conducted at 450 °C and 3 MPa, they found that Ru/CeO_2-TPAOH catalyst had 22000 μmol g^{-1} h^{-1} of activity, while the values achieved for Ru/CeO_2-EDA and Ru/CeO_2-NaOH were 19000 μmol g^{-1} h^{-1} and 16500 μmol g^{-1} h^{-1}, respectively. They added that Cs and Ba promoters were able to increase the activity of Ru/CeO_2-TPAOH catalyst, while K promoters had a reverse effect on it. 32000 μmol g^{-1} h^{-1} of activity was achieved for 4 % Cs- 2.5 % Ru/CeO_2-TPAOH catalyst. The possible reasons for the activity performance of Ru/CeO_2-TPAOH catalyst included large oxygen vacancy, 5.5 nm average pore size, high specific surface area.

2.1.4. Cobalt-based Catalysts

Inoue *et al.* [45] found that Co catalyst performance could be enhanced by the addition of $12CaO.7Al_2O_3$ electride. Moreover, it was found that Co/C12A7:e^- catalyst had an activation energy that was significantly lower than that of Co/C12A7:O^{2-}. The activation energy was comparable to those of Co_3Mo_3N and LiH-Co catalysts. The study concluded that Co, which is not highly active by itself could be enhanced by the compound presented.

Tarka *et al.* [46] prepared various catalysts supported with Carbon and promoted with Barium. The Cobalt amount was kept the same (27.4 wt%) but Barium content was varied. Barium was found to be rather effective when Cobalt catalyst was supported with Carbon. A tiny amount of Barium addition was found to influence the Cobalt active phase in a good way. Sintering was found to decrease, alongside with the prevention of the methanation of the support.

2.1.5. Kinetics

A well-known rate equation was proposed by Temkin and Pyzhev in a study conducted in 1940 [47], in an effort to propose a rate equation based on promoted iron catalysts.. The equation was reported to have been used for correlation of various experimental data [48]. Temkin and Pyzhev initially used partial pressures in derivation, instead of fugacities of the species present, which led to the exclusion of real conditions as reported by Nielsen *et al.* [48] and the rate equation became

$$r = k_1 P_{N_2} \left(\frac{P_{H_2}^3}{P_{NH_3}^2} \right)^{\alpha} - k_2 \left(\frac{P_{NH_3}^2}{P_{H_2}^3} \right)^{\beta} . \tag{2.1}$$

In a study Temkin later conducted in 1950, he modified the rate equation above so that it would be suitable for higher pressures. He included the pressure effects on adsorption and desorption terms rate constants. The new equation now contained fugacity terms in places of partial pressure terms and was given as [48, 49]

$$r = \left[k_1^o a_{N_2} \left(\frac{a_{H_2}^3}{a_{NH_3}^2} \right)^{\alpha} - k_2^o \left(\frac{a_{NH_3}^2}{a_{H_2}^3} \right)^{\beta} \right] e^{\left(-\frac{P(V_a - \alpha V_s)}{RT} \right)} , \tag{2.2}$$

where V_a and V_s represented partial molar volume of the nitrogen that was adsorbed and the partial molar volume of the transition state [48].

Nielsen *et al.* tried to find six unknown coefficients by his experiments conducted with KM1R catalyst produced by Topsoe. The detailed results can be found in their study. The formulated rate equation was given as [48]

$$r = \frac{k_2^o \left(a_{N_2} K_a^2 - \frac{a_{NH_3}^2}{a_{H_2}^3} \right)}{\left(1 + K_3 \frac{a_{NH_3}}{a_{H_2}^w} \right)^{2\alpha}} , \tag{2.3}$$

where the rate parameters were reported as

$$k_2^o = k_{20} e^{\left(-\frac{E_2}{RT} \right)} , \tag{2.4}$$

$$K_3 = K_{30} e^{\left(-\frac{E_3}{RT}\right)}, \tag{2.5}$$

and

$$log_{10} K_a = 2.6899 - 2.691122 log_{10} T - 5.519265x10^{-5} T + 1.848863x10^{-7} T^2 + \frac{2001.6}{T}. \tag{2.6}$$

Imamura *et al.* [50] examined Ruthenium based catalysts supported on Pr_2O_3 , MgO , CeO_2 . It was deduced in the work that the effect of nitrogen with respect to partial pressure varied within a small interval of unity, which led to the conclusion that the bond cleavage of nitrogen molecules is the rate-determining step. The effect of hydrogen on rate equations largely varied and the highest reaction order with respect to hydrogen was observed on Pr_2O_3 supported Ru-based catalyst (0.43), while the lowest reaction rate with respect to hydrogen was observed on MgO supported Ru-based catalyst (-0.92). The fact that there was a large variation in the results was attributed to more possible hindering effect of hydrogen poisoning. Power law rate equation form and corresponding powers of the components is given below. Reaction order with respect to ammonia is negative, so it's in denominator, hindering the rate equation as it is being produced. Data as to the reaction orders for different Ruthenium based catalysts could be found in the table presented in their work, with the rate equation given as

$$r = k P_{N_2}^{n} P_{H}^{h} P_{NH_3}^{a}. \tag{2.7}$$

The well-known kinetic expression for the rate equation, developed by Sehested *et al.* for the reduced form of KM1 catalysts, named KM1R, was given as [51]

$$r = 2N_s K_1 k_2 \theta^2 \left(P_{N_2} - \frac{P_{NH_3}^2}{P_{H_2}^3 K_{eq}} \right), \tag{2.8}$$

where the parameter θ was reported as

$$\theta = \left(1 + \frac{P_{NH_3}}{P_{H_2}^{1.5} K_a} + \frac{P_{H_2}^{0.5}}{K_b} \right)^{-1}. \tag{2.9}$$

The results were the factor in the rate equation given in Arrhenius form by Zhang *et al.*, and they are retabulated here with the same formula [51, 52] given as

$$Arrhenius\ form = A\, e^{\left(-\frac{E_a}{RT}\right)}. \tag{2.10}$$

Table 2.1. Rate parameters used for iron-based KM1 catalyst.

Kinetic Parameters	Units	Pre-exponential factor A	Activation energy E_a (kJ mol^{-1})
$2N_sK_1k_2$	μmol gcat^{-1} s^{-1} bar^{-1}	7.79×10^3	6.6
K_{eq}	bar^{-2}	2.03×10^{-12}	-101.6
K_a	bar$^{-0.5}$	2.70×10^{-2}	27.1
K_b	bar$^{0.5}$	2.16×10^3	48

2.2. Unconventional Ammonia Synthesis

This chapter focuses on the unconventional ammonia synthesis. By unconventional, it is meant that the methods are unlike the traditional Haber-Bosch process carried out by industrial well-known catalysts at high temperature and pressure.

Electrochemical ammonia synthesis is a method to produce ammonia in mild conditions, where the use of renewable electricity is implemented. The method has gained a lot of attraction due to the reasons that it has potential to be more efficient than Haber-Bosch process, it can be augmented in its cleanness via implementation of various renewable energy sources, it can use the hydrogen from water oxidation, it can be easily controlled via the adjustment of external voltage, it is suitable for operations focused on small-scale. The aim to reduce the operation temperatures between 100 and 500 °C is hindered by the requirement of large potential differences, which renders the efficiency lower. The studies are still ongoing to enhance the process [53].

Biocatalytic ammonia synthesis has also gained attention due to the potential of being more efficient than Haber-Bosch process. Nitrogenase, an enzyme produced by bacteria has evolved to produce ammonia at mild conditions of ambient pressure and ambient temperature [54]. The aim to create a catalyst that is like nitrogenase was reported be a still ongoing study [55].

2.3. Sorption Enhanced Ammonia Synthesis

An enhancement to the process can be made by a modification to Haber-Bosch process. Nikacevic *et al.* [56] modeled a configuration in which solid absorbents that were selective to ammonia were present. The idea was to surpass the thermodynamic limitations. Ammonia, which is the sole product of the reaction, is absorbed to drive the reaction forward. They reported that about 2.2 times better conversion values were obtained in their simulation. Even if lower operating pressure is chosen, high conversion values would still be achievable. Moreover, an interesting observation was that when inlet temperature was lower, better conversion values were obtained due to adsorption being more effective at lower temperatures. Therefore, the method was suggested to be a cost-saving one in terms of the lack of the need for high pressure and temperature.

2.4. Membranes and Membrane Reactors

Membrane reactor is a configuration that can be implemented if the reaction is limited by thermodynamics. For exothermic reactions, the increase in the rate of reaction resulting from the increase in temperature comes with the cost of decreased conversion of the reactants. Unlike endothermic reactions, there is a trade-off. The implemented membrane can allow one to surpass thermodynamic limits by allowing certain components to pass through [57].

Various types of membranes have been examined for ammonia synthesis so far with the purpose of reducing the impacts of thermodynamic limitations. A recent study by Wei *et al.* provided information regarding permeance and selectivity values on ZIF-21, a metal-organic framework (MOF) material. They found out that a very high permeance value of 1727 GPU was achievable for ZIF-21, while selectivities of 35 for ammonia/nitrogen and 12 for ammonia/hydrogen were observed at ambient conditions. However, the lack of data at the high temperatures (~400-500 ºC) of ammonia synthesis limits the adoption of ZIF-21 into reactor simulations adjusted to operate at harsher conditions [58].

Bhown and Cussler [59] tried to express the mechanisms through which ammonia diffuses within membranes. These were given as sorption, mobile carrier, and chain carrier mechanisms. It was seen in the experiment that poly(vinyl-ammonium thiocyanate) membrane's ammonia selectivity could be 3000 times more than its selectivity for nitrogen and hydrogen. However, the membrane's temperature durability is rather weak since it was suggested in the work that decomposition would occur above 170 ºC.

Cussler and He [60] found that at 200 ºC the permeability of ammonia in Nafion membranes was around 25 barrer at most, a value quite small, even though the selectivity of ammonia over nitrogen was over 3000. This study lacks the data at higher temperature, which is necessary for our system since the kinetics require higher temperature even when a membrane is integrated.

Another study on silica membranes carried out by Kanezashi *et al*. [61] found out that these membranes were highly stable without any drop in their permeances even at 400 ºC. However, selectivities over nitrogen and hydrogen were quite small, which is not what we want in our model.

In addition to the polymeric/MOF-based ones, inorganic membranes were also investigated for selective separation of ammonia. These membranes have the unique advantage of being compatible with the high temperatures of ammonia synthesis. The study carried out by Laciak *et al*. [62] provided valuable information on experimentally measured permeance and selectivity values for $ZnCl_2$-IMS type membranes at temperatures between 250 ºC and 350 ºC. It was also seen in the experiment that even after intense operation carried out continuously for 21 days, there was no decline in the membrane performance. Selectivities were proven to be excellent, it was estimated in the work that the selectivity of ammonia over nitrogen was at least 1000. Similarly, the selectivity of ammonia over hydrogen was predicted to be at least 3000. Based on these observations, our assumption that the model only accounts for the passage of nitrogen through the membrane in the model is justified. However, for implementation of the membrane between the reaction channel and the permeate channel, the membrane must be supported with some kind of cloth. The data at 311 ºC is available for $ZnCl_2$ IMS membrane that is supported with Zirconia cloth material, rendering its thickness to 0.38 cm, a remarkable increase over 0.02 cm, which is what the thickness was without any clothing in the experiment.

Zhang *et al*. [52] investigated membrane reactor for ammonia synthesis. They simulated a packed bed tubular reactor with an imaginary membrane having various ammonia permeability. They found that ammonia permeance had to be higher than 100 GPU in their configuration to achieve promising results in terms of conversion and ammonia recovery. They also denoted that this phenomenon held true until a permeance of 1000 GPU, above which they obtained no significant gain. They also mentioned that minimum ammonia selectivity of 4 and 10 over hydrogen and nitrogen was needed. However, the ideal selectivities of over 10 were preferable. When the ammonia selectivities over hydrogen and nitrogen were higher than 10, the conversion and ammonia recovery essentially did not depend on selectivity. They also denoted that pressure was an important factor, with pressure driving the conversion values further as it increased. Temperature was found to have similar effects in terms of conversion. Overall, they expressed that their configuration could be operated at 300 ºC while displaying better performance over a packed-bed reactor without a membrane operating at 400 ºC.

3. MATHEMATICAL MODELING

Architecture of the cooling integrated microchannel MR is illustrated in Figure 3.1. The stainless–steel reactor block comprises rectangular reaction (R) and permeate (P) channels with identical cross–sectional dimensions of 3×10^{-4} m (H) and 6×10^{-4} m (W) determined by taking the trade–off between transport coefficients and pressure drop [63]. Exothermic heat released within the reaction channels is absorbed by the permeate gas that also functions as a coolant flowing in the neighboring permeate channels. Channel length (L) is taken as 1.5×10^{-1} m. The bulk iron catalyst (commercial KM1 catalyst manufactured by Haldor Topsøe A/S; composition: 94% Fe, 2.8% CaO, 2.5% Al_2O_3 and 0.6% K_2O ([64])) is considered as a thin layer that is coated uniformly to the interior x–z surface of each reaction channel. Layers of the catalyst and the membrane are located to face each other (Figure 3.1). Properties of the KM1 catalyst are adopted from the literature [52], [65, 66]. The rate equations for the catalyst were given by Equation (2.8), Equation (2.9), and Equation (2.10). The parameters for the catalyst were given in Table 2.1.

Table 3.1. Physical properties of the iron-based KM1 catalyst.

Property	Value	Reference
Catalyst density (kg m^{-3})	4.8×10^{3}	[52]
Porosity of the catalyst layer (ε_{cat}, –)	0.44	[52]
Tortuosity† (τ_{cat}, –)	3.3	[65]
Pore diameter†† (d_{pore}, m)	51.8×10^{-9}	[66]

†Approximated with that of commercial (Haldor Topsøe A/S) methanol synthesis catalyst.

††Approximated with that of a Fe_3O_4 catalyst.

Note that the parameters required for the calculation of diffusion coefficients were replaced by those of an approximate catalyst, as the search for the complete information on the KM1 catalyst did not yield all of the numerical values required for the modeling of the system. Therefore, the need for obtaining similar results arised. Tortuosity and pore diameter values were gathered for a different catalysts and adopted as the same here.

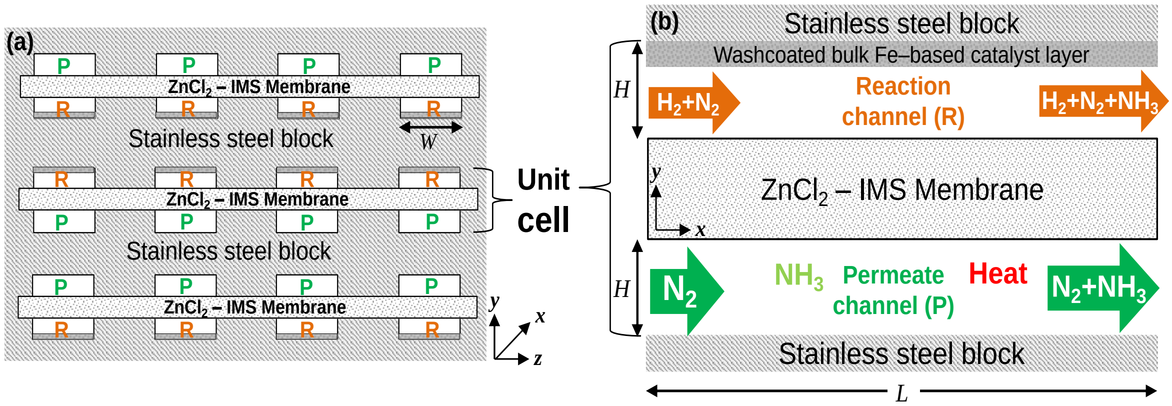

Figure 3.1. Illustration of the (a) cooling integrated microchannel MR and (b) the characteristic repeating unit of the multichannel reactor in 2D. The number of permeate (P) and reaction (R) channels in MR is determined by the capacity; they are not necessarily limited to a total of 24 as shown in (a).

As presented in Figure 3.1, reaction and permeate channels are physically segregated by layers of NH_3 permselective membrane. Laciak *et al.* [62] studied NH_3 separation from H_2 and N_2 on a 3.8×10^{-3} m thick zirconia supported $ZnCl_2$ IMS membrane at 584 K. They reported NH_3/N_2 and NH_3/H_2 selectivities above 3×10^3 and 1×10^3, respectively, and NH_3 permeability between $2.2–7\times10^5$ barrer. In addition to its superior selectivity features, the membrane can remain stable and functional until up to 623 K [62]. Based on these data, zirconia supported $ZnCl_2$ IMS is considered as the membrane which is decorated between the permeate and reaction channels. Laciak *et al.* [62] also showed that the permeability of NH_3 across the membrane decreases by increasing its partial pressure and temperature. Outcomes of the simulations carried out in the absence of membrane (see Results and Discussion) show that the mole fraction of NH_3 in the reaction mixture remains around $\sim7.5\times10^{-2}$. This composition allows the use of the highest NH_3 permeability value of 7×10^5 barrer. However, this data was reported at 584 K, and the temperature is allowed to increase until 623 K, the maximum operating temperature of the $ZnCl_2$ IMS membrane, in our simulations. Considering the negative impact of temperature and the multicomponent nature of the reaction mixture that may hinder cross membrane transport, NH_3 permeability is taken as 6×10^5 barrer (equivalent to ~160 GPU on a 3.8×10^{-3} m thick membrane) in the current study.

Location of the reaction and permeate channels in Figure 3.1(a) sets the basis for the simplification of the multichannel reactor block operation to that of the unit cell presented in Figure 3.1(b). In this context, (a) heat transport between identical channels is ignored and takes place only between the reaction and permeate channels in x and y coordinates, (b) heat exchange across the outermost boundaries of the reactor block is neglected, and (c) reaction mixture ($N_2 + H_2$) and the permeate gas (N_2) are dosed evenly to the pertinent channels. The latter assumption of uniform flow partitioning is based on the existence of identical channel dimensions and the uniform catalyst coating thickness, both of which are possible by the applicability of high precision micro–machining and reproducible catalyst coating techniques [67]. Base–case operation scenario of the unit cell (Figure 3.1(b)) involves steady–state, co–current feeding of the reactant and permeate gases at identical temperature and pressure of 613 K and 50 bar, respectively, and the space velocity of 1.5×10^3 m^3 kg_{cat}^{-1} s^{-1}. The default inlet molar flow rate of the permeate gas is taken as 50 times of that of the reaction mixture. In addition to these parameters, the effects of the composition of the reaction mixture (molar inlet H_2/N_2 ratio) and the difference between the inlet temperatures of the reaction and permeate channels on reactor performance are investigated. Pressure gradient between the channel inlets is nullified (Section 4.5 adds detail about the problems)due to (a) its negligible impact in the performance of membrane integrated reactors similar to the current one [68, 69], (b) elimination of technical complexities in adjusting pressures to permeate and reaction channels, and (c) possible mechanical damages of the membrane layer due to pressure difference. Default values and the ranges of these parameters (Table 3.2) are determined such that temperature increase due to exothermic nature of reaction remains below 623 K, the thermal stability limit of the membrane [62]. This condition can be satisfied only by co–current flow partitioning as the intense heat release at the reactor inlet can be regulated by dosing the cold permeate gas in the same spatial frame. In this regard, the inoperable counter–current flow configuration is not considered. Moreover, one can expect a performance drop in the operation of membrane when counter-current operation is chosen, as it will be harder if not impossible for the ammonia to pass through from reaction channel to permeate channel in the beginning of the reaction, where the reaction is expected to be fastest. As the configuration involves both heat transfer and mass transfer, one should choose the settings for which the total gain will be the highest. Co-current operation is the setting one should opt for here.

Table 3.2. Default values and ranges of the operating parameters.

Parameter	Default value	Range
T_{in}^{R} (K)	613	583–613 (583, 593, 603, 613)
$\Delta T_{in} = T_{\text{in}}^{\text{R}} - T_{\text{in}}^{\text{P}}$ (K)	0	0–20 (0, 10, 20)
p_{in}^{R} (bar)	50	30–50 (30, 40, 50)
Molar inlet H_2/N_2 ratio (–)	3	2–4 (2, 3, 4)
Space velocity (ratio of the volumetric flow rate of reactants to the mass of catalyst bed) ($\times 10^3$ m^3 $\text{kg}_{\text{cat}}^{-1}$ s^{-1})	1.5	1.5–6 (1.5, 3, 4.5, 6)
Ratio of the permeate channel inlet molar flow rate to the reaction channel inlet molar flow rate ($F_{\text{in}}^{\text{p}}/F_{\text{in}}^{\text{R}}$, –)	50	10–50 (10, 20 ,30, 40, 50)

The bulk iron catalyst KM1 is immobilized as 5×10^{-5} m thick layers into the reaction channels (Figure 3.1). The layer thickness is determined such that intra–layer mass and heat diffusion limitations remain negligible [67]. N_2 conversion is assumed to be driven by the iron–based catalyst; gas–phase reactions and any possible catalytic effects due to membrane and reactor materials are neglected.

Simultaneous reaction, cooling and membrane separation in the domain of the unit cell at steady–state (Figure 3.1(b)) is modeled by the solution of mass, momentum and energy conservation equations in the fluid phases of the reaction and permeate channels, reaction in the coated catalyst layer and NH_3 transport across the $ZnCl_2$ IMS membrane. Conservation equations and accompanying empirical correlations for the estimation of fluid properties are provided in Table 3.4 and 3.5. The model is constructed in two spatial dimensions (x and y coordinates) and the variations in the z coordinate are not taken into account. Omission of the third spatial dimension is justified by the negligible differences between the outcomes of two and three dimensional models constructed for an *in–situ* cooled wall coated microchannel reactor that is very close to the configuration presented in Figure 3.1 [70]. The reactive mixture and the permeate gas are modeled as Newtonian fluids and assumed to follow ideal–gas law behavior. This assumption has been justified by incorporating ideal and real–gas (Soave–Redlich–Kwong, SRK) equation of states to the mathematical model and solving them. Close outcomes of the solutions presented in Section 4.1 clearly allow the adoption of ideal–gas behavior, which significantly reduces computation cost. Moreover, fluids are assumed to be incompressible due to the negligible (< ~1%) frictional pressure loss along the channels. Partial differential equations of the reactor model are solved numerically by the finite volume method run under ANSYS (v. 19.2) platform according to the boundary conditions specified in SI. In this context, the solution domain (Figure 3.1(b)) is meshed with the finest possible configuration allowed by the software and discretized with 5.76×10^{5} square cells, each of which has an edge length of 1.25×10^{-5} m. Therefore, the mesh independency of the results is not considered.

Modeling of NH_3 transfer across the $ZnCl_2$ IMS membrane is based on Fick's Law which has been incorporated into the reactor model equations by the methodology comprehensively described in the previous studies [68, 69]. Membrane operation and reaction kinetics (Equation (3.1) and Equation (2.8)) have been coupled with the ANSYS platform by means of user defined functions (UDF) adjusted as

$$J_{\mathrm{NH_3}} = Perm_{\mathrm{NH_3}}\left(p_{\mathrm{R}}^{\mathrm{NH_3}} - p_{\mathrm{P}}^{\mathrm{NH_3}}\right). \tag{3.1}$$

The resulting mathematical model is used to study the effects of the operating parameters and *in–situ* NH_3 withdrawal on reactor performance. For this purpose, the specific operating parameter is changed within its range by keeping the others fixed to their default values given in Table 3.2. The results are benchmarked with the cases in which membrane operation is disabled by considering an impermeable, 3.8×10^{-3} m thick wall between the channels. In this case, membrane layer in Figure 3.1 is replaced with the stainless–steel reactor material through which only heat flow occurs and the permeate gas flow is used only for regulating the exothermic temperature rise. Reactor performance is quantified in terms of per cent N_2 conversion, effluent NH_3 flow rate and reaction channel temperature, which are respectively based on the cross–sectional surface averaged N_2 and NH_3 molar flow rates, and temperature; with the N_2 conversion reported as

$$N_2\ conversion\ \left(x_{\mathrm{N_2}}, \%\right) = \frac{F_{\mathrm{N_2,in}} - F_{\mathrm{N_2,out}}}{F_{\mathrm{N_2,in}}}\ x\ 100. \tag{3.2}$$

Additionally, per cent N_2 conversion at thermodynamic equilibrium is computed as another benchmark to assess the capability of the membrane–integrated operation in approaching to / overcoming the natural limits of NH_3 synthesis. The equilibrium calculations included the extent of reaction, ξ, for simplicity. Partial pressures of the species require the mole fractions y_i to be introduced. The algorithm is provided as follows.

Table 3.3. Molar amounts and fractions of the species.

Species	Initial amount (mol)	Consumed or produced amount (mol)	Amount after reaction (mol)	Mole fraction (y_i)
N_2	$F_{\mathrm{N_2,in}}$	$-\xi$	$F_{\mathrm{N_2,in}} - \xi$	$(F_{\mathrm{N_2,in}} - \xi)/F_{\mathrm{T}}$
H_2	$F_{\mathrm{H_2,in}}$	-3ξ	$F_{\mathrm{H_2,in}} - 3\xi$	$(F_{\mathrm{H_2,in}} - 3\xi)/F_{\mathrm{T}}$
NH_3	-	2ξ	2ξ	$2\xi/F_{\mathrm{T}}$
		Total amount (mol)	$F_{\mathrm{T}} = F_{\mathrm{N_2,in}} + F_{\mathrm{H_2,in}} - 2\xi$	

The partial pressures of the species are calculated as

$$p_i = y_i p, \tag{3.3}$$

where p stands for the operating pressure. Utilizing the extent of reaction, one proceeds to the equilibrium calculations with the formula

$$K_{eq} = \frac{p_{\mathrm{NH_3}}^2}{p_{\mathrm{H_2}}^3 p_{\mathrm{N_2}}} = \frac{4\xi^2}{(F_{\mathrm{H_2,in}} - 3\xi)^3 (F_{\mathrm{N_2,in}} - \xi)} \frac{F_T^2}{p^2} \ . \tag{3.4}$$

Temperature dependent equilibrium constant parameters were provided in Table 2.1. Values of N_2 conversion at thermodynamic equilibrium are calculated for the membraneless cases (labeled as M- in in the thesis) in which the change (increase) in the reaction channel temperature from the inlet remains < ~5 K. In this regard, arithmetic average of the inlet and exit temperatures have been used in thermodynamic analysis calculations. For example, equilibrium N_2 conversion of 40% reported at the inlet temperature of 613 K in Figure 4.5 in the manuscript was calculated at 614.5 K, the arithmetic average of 613 K and 616 K (the exit temperature for the membraneless case reported in Figure 4.5(a)). In this specific case, Reactor pressure ($p = p_{\mathrm{in}}^{\mathrm{R}}$) is 50 bar and the $F_{\mathrm{H_2,in}}/F_{\mathrm{N_2,in}} = 3$. The resulting non–linear equation (Equation (3.4)) is solved numerically using the *fsolve* function in MATLAB (v. R2021a).

The equations of the mathematical model involving conservations of the mass, momentum and energy within the domain of the unit cell of the membrane integrated wall coated microchannel reactor (Figure 3.1(b)) is presented in Table 3.4.

Note that a wide range of equations are needed to fully represent the system. Intensive energy balance equations are needed to capture the heat effects of the system, as the heat transfer between the reaction channel and the permeate channel and the heat generated by reaction in the catalyst zone is balanced here by the steady state assumption.

Although the mechanism of heat transfer is mostly convective, there is also conductive heat transfer through the membrane layer, as the solid layer allows the passage of both mass and energy. Another steady state assumption is made for the membrane layer, meaning that there is no temperature gradient in the membrane layer over time, which is the need for continuous operation for a long period of time.

One should also note that the momentum balance equations differ for the catalyst phase and the fluid phase. Another important point is that the mass transfer equations contain not only the convective and diffusive terms, but they also capture the rate effects for each species involved in the reaction. This means that there must be three additional equations relating the rate of reaction to the production or consumption of the species involved in the reaction. As there is a single reaction going on here without any side reaction occurring, the task is simple.

Modeling of fluid requires extensive thermodynamic relationships which must be provided to the mathematical modeling. Table 3.5 summarizes all of the thermodynamic relationships used in this study. As discussed in Section 4, the study employs ideal gas model for the behavior gases.

One should also note that the model employs extensive diffusivity relations, allowing for the comprehensive calculations for the behavior of gases in the system. These are needed as the gases in the system has different regions along which they flow. The regions are named as the catalyst phase and the fluid phase. The equations were provided to ANSYS platform to obtain detailed results for all the simulations presented in Section 4.

Table 3.4. Equations of the reactor model.

Continuity equation	$\rho_m \nabla . \vec{\boldsymbol{v}} = 0$	(3.5)
Momentum equation (FP)	$\rho_m \nabla . (\vec{\boldsymbol{v}}\vec{\boldsymbol{v}}) = \nabla p + \mu_m \nabla . \left[\left(\nabla \vec{\boldsymbol{v}} + (\nabla \vec{\boldsymbol{v}})^T - \frac{2}{3}(\nabla . \vec{\boldsymbol{v}})I\right)\right]$	(3.6)
Momentum equation (CP)	$\rho_m \nabla . (\vec{\boldsymbol{v}}\vec{\boldsymbol{v}}) = \vec{\boldsymbol{F}} - \nabla p + \mu_m \nabla . \left[\left(\nabla \vec{\boldsymbol{v}} + (\nabla \vec{\boldsymbol{v}})^T - \frac{2}{3}(\nabla . \vec{\boldsymbol{v}})I\right)\right]$ $\vec{\boldsymbol{F}} = -\left(\frac{\mu_m}{\alpha}\vec{v} + \frac{C_2}{2}\rho_m \lvert\vec{v}\rvert\vec{v}\right); \alpha = \frac{d_{\text{part}}^2}{150}\frac{\varepsilon_{\text{cat}}^3}{(1-\varepsilon_{\text{cat}})^2};\ C_2$ $= \frac{3.5}{d_{\text{part}}}\frac{(1-\varepsilon_{\text{cat}})}{\varepsilon_{\text{cat}}^3}$	(3.7)
Species mass equation (FP)	$\rho_m \nabla . (\vec{v} Y_i) = -\nabla . \vec{J_\iota}$ $\vec{J_\iota} = -\rho_m D_{i,m} \nabla Y_i\ ;\quad (i = \mathrm{N_2}, \mathrm{H_2})$ $\vec{J_\iota} = -\rho_m D_{i,m} \nabla Y_i - Perm_i\left(p_{\mathrm{R}}^i - p_{\mathrm{P}}^i\right); (i = \mathrm{NH_3})$	(3.8)
Species mass equation (CP)	$\rho_m \nabla . (\vec{v} Y_i) = -\nabla . \vec{J_\iota} + M_i R_i$ $\vec{J_\iota} = -\rho_m D_{eff,i,m} \nabla Y_i;\quad (i = \mathrm{N_2}, \mathrm{H_2})$ $\vec{J_\iota} = -\rho_m D_{eff,i,m} \nabla Y_i - Perm_i\left(p_{\mathrm{R}}^i - p_{\mathrm{P}}^i\right); (i = \mathrm{NH_3})$ $R_{\mathrm{NH_3}} = 2r\ ;\ R_{\mathrm{N_2}} = -r;\ \ R_{\mathrm{H_2}} = -3r$	(3.9)
Energy equation (FP)	$\rho_m c_{p,m} \nabla . (\vec{v}\, T) = k_m \nabla . (\nabla \mathrm{T})$	(3.10)
Energy equation (CP)	$\rho_m c_{p,m} \nabla . (\vec{v}\, T) = k_{eff,m} \nabla . (\nabla \mathrm{T}) + (-\Delta H)(r)$	(3.11)
Energy equation (ML)	$k_w \nabla . (\nabla \mathrm{T}) = 0$	(3.12)

Equation (3.12) is used to compute heat flux through sodalite membrane layer decorated between permeate and reaction channels. In the membrane integrated cases, the wall material is simulated as ZrO_2, the support material of the membrane. In the membraneless cases (where no interchannel mass transfer occurs), the wall material is considered as stainless steel.

Table 3.5. Empirical correlations and mixing laws.

Property	Correlation/mixing law	Reference
Mixture viscosity (3.13, 3.14)	$\mu_m = \sum_{i=1}^{N_g} \frac{y_i \mu_i}{\sum_{j=1}^{N_g} y_j \phi_{ij}},$ $\phi_{ij} = \frac{1}{\sqrt{8}}\left(1+\frac{M_i}{M_j}\right)^{-1/2}\left[1 + \left(\frac{\mu_i}{\mu_j}\right)^{1/2}\left(\frac{M_j}{M_i}\right)^{1/4}\right]^2$	[71]
Thermal conductivity of reactive mixture (3.15)	$k_m = \sum_{i=1}^{N_g} \frac{y_i k_i}{\sum_{j=1}^{N_g} y_j \phi_{ij}}$	[72]
Effective thermal conductivity of the reactive mixture within the catalyst layer (3.16)	$k_{eff,m} = \varepsilon_{\mathrm{cat}} k_m + (1-\varepsilon_{\mathrm{cat}}) k_{cat}$	[72]
Diffusivity of species *i* in the mixture (3.17)	$D_{i,m} = \frac{1-y_i}{\sum_{j=1}^{N_g} y_j / D_{ij}}, j \neq i$	[73]
Binary diffusivity (3.18)	$D_{ij} = \frac{10^{-3} T^{1.75}\left(\frac{1}{M_i}+\frac{1}{M_j}\right)^{1/2}}{p\left[(\sum \upsilon)_i^{1/3} + (\sum \upsilon)_j^{1/3}\right]^2}$	[74]
Effective diffusivity of species *i* in the catalyst layer (3.19)	$D_{eff,i,m} = \frac{\varepsilon_{\mathrm{cat}}}{\tau_{\mathrm{cat}}}\left[\frac{1}{D_{K,i}} + \frac{1}{D_{i,m}}\right]^{-1}$	[75]

Table 3.5. Empirical correlations and mixing laws (cont.).

Knudsen diffusivity for species i (3.20)	$D_{K,i} = 48.5 d_{\text{pore}} \sqrt{\frac{T}{M_i}}$	[75]
Mixture heat capacity (3.21)	$c_{p,m} = \sum_{j=1}^{N_g} c_{p,i} y_i$	-
Density and molecular weight of the mixture (3.22)	$\rho_m = \frac{P M_m}{RT}, M_m = \sum_{j=1}^{N_g} M_i y_i$	-

4. RESULTS AND DISCUSSION

4.1. Verification of the Mathematical Model with Experimental Data

Prior to its use in elucidating the effects of *in–situ* separation of NH_3 on its synthesis, the mathematical model is benchmarked with the literature–based experimental data. The reported data is selected by considering the similarity of the catalyst type and operating conditions to the current ones presented in Table 3.2. In this regard, data reported by Rosowski *et al.* [76], all obtained on the commercial iron–based catalyst considered in this study, are considered as the reported space velocity range of 4.2–17.3×10^3 mL g_{cat}^{-1} h^{-1} is close to 5.4–21.6×10^3 mL g_{cat}^{-1} h^{-1} (equivalent to 1.5–6×10^{-3} m^3 kg_{cat}^{-1} s^{-1}) involved here. The current pressure range of 30–50 bar (Table 1) falls within 1–107 bar of the experiments, all of which are conducted at 673 K, <10 % above that of the default inlet temperature of 613 K[76]. In all comparisons, the inlet molar composition is always kept constant at $H_2/N_2 = 3$. As the experimental data are produced in isothermal packed–bed reactors without membrane, the integrated separation and cooling functions are disabled in the mathematical model of the wall–coated microchannel reactor. Despite their different architectures, both reactors are comparable due to existence of intrinsic catalytic response.

Comparison of the model outputs and experimental data in terms of the outlet NH_3 concentration are presented in Figure 4.1. The results point out 15–20% difference in favor of the model predictions. While the well–defined flow path of the simulated structured reactor offers a sharp residence time distribution (RTD) ensuring the uniformity of residence time and higher conversions, the inherently less uniform RTD feature of the packed–bed architecture involved in the experimental studies might have decreased the reactor performance. This explanation is supported by comparisons of cases B–D in Figure 4.1 pointing out closer prediction of the experimental data at higher space velocities that homogenize duration of contact between the reactive mixture and the catalyst leading to narrower RTD and elevate NH_3 concentration. A supplementary evidence is the occurrence of the same difference (~15%) in cases A and D having nearly identical space velocity of ~17×10^3 mL g_{cat}^{-1} h^{-1} (Figure 4.1).

The current model is based on ideal behavior of the gases. In this regard, the model is also based on SRK equation of state to assess whether the deviations could be due to the ideal gas assumption or not. Model outcomes based on the real gas behavior are presented in Figure 4.1 for cases B–D (107 bar data). The results show that the difference between adoption of ideal and real gas conditions causes a difference less than only 0.5%, which justifies the use of ideal gas equation of state in the current study and proves that the gaps between the model and experiment are not related to the ideal gas assumption. This statement is further validated by the identical gap of ~15% in cases A and D involving pressures of 1 and 107 bar, respectively. These simulations assume incompressible fluid flow. Validity of this assumption is investigated by executing the model with the compressible fluid approach at the default conditions presented in Table 3.2. The identical N_2 conversions of 47.4% obtained in both cases clearly show that the change in the density of the fluid with pressure is negligible, and also pressure drop along the reactor is negligible. Furthermore, the mathematical model, customized with the SRK equation of state and the compressible fluid approach, gives N_2 conversion 47.3% (at the default conditions in Table 1) which almost the same with that obtained from the model involving ideal gas equation of state and the incompressible fluid approach. In the light of these findings, the mathematical model based on ideal gas and incompressible fluid assumptions, and the reaction kinetics provided in Equation (2.8) are used in analyzing the characteristics of the membrane and heat–exchange integrated microreactor.

Only after explaining the validity of the kinetic model, which is of utmost importance as it determines the performance of all the aspects of the dynamics of the overall model, is one able to proceed to examine the characteristics of the all the parameters in the reaction. These parameters can include many factors, with the most basic ones being the inlet temperature of the gases and the inlet pressure of the gases. However, with a system as complicated as the one presented here, one can examine many others, including the permeate gas molar flow rate, the inlet space velocity, the temperature difference between the reaction channel and permeate channel, and the molar flow rate ratio of the reaction channel gases. All of these factors are examined in this study and discussed in detail in order to capture the complete characteristics of the reactor model.

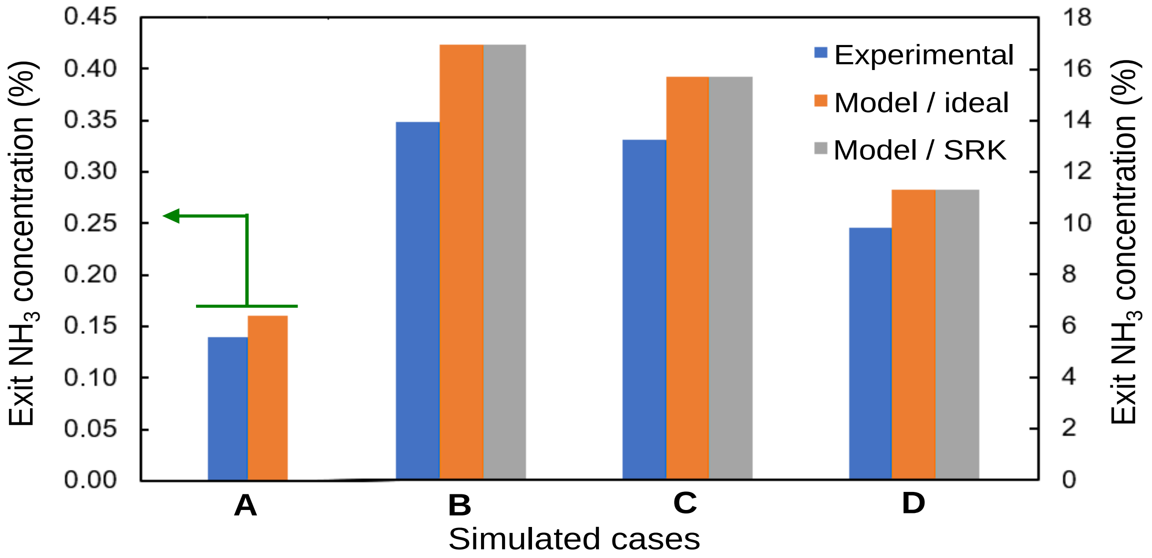

Figure 4.1. Experimental [76] and computed values at the reactor exit (T_{in}^{R} = 673 K, H_2/N_2 = 3), (A: p_{in}^{R} = 1 bar, space velocity = 17.0×10^{3} mL g_{cat}^{-1} h^{-1}; B: p_{in}^{R} = 107 bar, space velocity = 4.2×10^{3} mL g_{cat}^{-1} h^{-1}; C: p_{in}^{R} = 107 bar, space velocity = 5.9×10^{3} mL g_{cat}^{-1} h^{-1}; D: p_{in}^{R} = 107 bar, space velocity = 17.3×10^{3} mL g_{cat}^{-1} h^{-1}).

4.2. Effect of Changing Permeate Gas Molar Flow Rate

The inlet molar flow rate of permeate gas has been varied by changing the linear velocity of permeate gas flow rate, as the concentration of inlet molar flow rate of permeate gas is the same as the that of inlet molar flow rate of feed gas (613 K, 50 bar). Then, in order for one to change the molar flow rate, volumetric flow rate must be varied. However, the reaction and permeate channel cross sectional area is constant, which leads to the fact that one can easily adjust the linear velocity of permeate gas to set a different permeate gas molar inlet molar flow rate.

The default condition was set such that the inlet linear velocity of permeate gas was 50 times that of the feed gas, denoted here in the graphs simply as 50, representing the ratio of molar flow rate of the inlet permeate gas to feed gas. For investigation, the cases 40x, 30x, 20x, 10x were also included to see the effect of permeate gas molar flow rate on outlet conditions.

The strong dependence of the temperature profile to the permeate gas molar flow rate is evident in Figure 4.2. As more and more nitrogen flows through the permeate channel, the permeate channel of the reactor is able to capture and “sweep” more of the heat produced by the conversion of nitrogen and hydrogen to ammonia. As the permeate/feed inlet molar flow rate ratio increases, the permeate channel containing hot gas due to absorption of heat generated by the reaction is quickly replaced by the incoming colder permeate gas. This “quickness” decreases as the ratio is decreased, causing heat generated by the reaction to be trapped more along the reactor, hence more temperature increase.

In Figure 4.2 below, one can see the effect of permeate/feed inlet molar flow rate ratio effect on reactor temperature. Note that the ratio of 50 is the limit for the configuration presented here due to membrane temperature limitations. For $ZnCl_2$ - IMS membrane, with these operating conditions chosen, one risks the life expectancy of the membrane severely if the ratio is chosen to be below 50. In an extreme case, when the ratio 10, nearly 655 K is reached at reactor exit.

The trend is the same in the membraneless simulations as well. As the permeate/feed inlet molar flow rate ratio increases, temperature increase along the reactor decreases as well. However, in the absence of membrane, the rate of reaction along the reactor decreases rapidly due to thermodynamic limitations. Therefore, conversion of nitrogen decreases enormously compared to membrane-integrated simulations. This immense drop in conversion causes less heat to be generated along the reactor, which leads to milder temperature increase. However, the absence of membrane severely harms the efficiency when one examines the plots of 40 / M+ and 10 / M- below. Even though the reactor exit temperatures of these simulations topped out at nearly 626 K, overall temperature profile is lower in 40 / M+ simulation. Moreover, 40 / M+ achieved nitrogen conversion of 46.8%, while 10 / M- was able to achieve only 14.3%. The inevitability of membrane integration for better efficiency is justified.

Another important point worth noting is that membrane acts as a multiplier for temperature increase effect. The reader is encouraged to observe the difference between the plots of 50 / M+ and 10 / M+, and also between 50 / M- and 10 / M- . Although the increase in temperature as the ratio decreases is evident, the total changes in temperatures are not the same. Membrane breaks thermodynamic limitations and increases conversion enormously, thereby making it difficult to harness the temperature increase along the reactor.

Perhaps the most important point is the change of nitrogen conversion with the molar flow rate ratio. One might be confused as to why all simulations have the same nitrogen conversion in simulations including membrane. After all, the amount of ammonia that passes through the membrane from the reaction channel to permeate channel is expected to be more. This phenomenon holds true. We saw a slight increase in the total amount ammonia that passes through the membrane to the permeate channel. In 50 / M+ simulation, about 4.3% more ammonia has passed through the membrane to the permeate channel compared to 10 / M+ simulation. Negligible increase is owing to the fact that even when the permeate/feed inlet molar flow rate ratio is 10, ammonia was already rather diluted in the permeate channel, rendering its partial pressure very low. One might question the necessity of higher flow rate along the permeate channel. However, additional increase in the permeate/feed inlet molar flow rate ratio is required to keep the reactor temperature in control for the membrane and safely operate the configuration.

We have denoted so far that temperature is the main indicator of the reaction rate. However, the decrease in the permeate/feed inlet molar flow rate ratio for the simulations with membrane does not seem to increase the rate of reaction as one might expect it to even though temperature along the reactor increases (See Table 4.1 for nitrogen conversion values). Based on conversion values, one can easily say that we should have the same rate profiles. After all, the conversion is based on the rate profiles. Figure 4.3 shows that this is the case. The integral of the rate profiles are about the same, hence the same conversion values. The problem is that as the temperature increases more, the backward reaction, or the reaction of decomposing of ammonia to its constituent elements nitrogen and hydrogen kicks in, which prevents the forward rate of reaction from increasing further. In ANSYS, we obtained the same nitrogen conversion of 47.4% for 50 / M+, 40 / M+, 30 / M+, and 20 M/+. The result was 47.2% for 10 / M- (Table 4.1), indicating that the permeate/feed inlet molar flow rate ratio of some value about 20 is operating point at which there is no further gain in nitrogen conversion. A better membrane with more ammonia permeance capability is required to obtain better results.

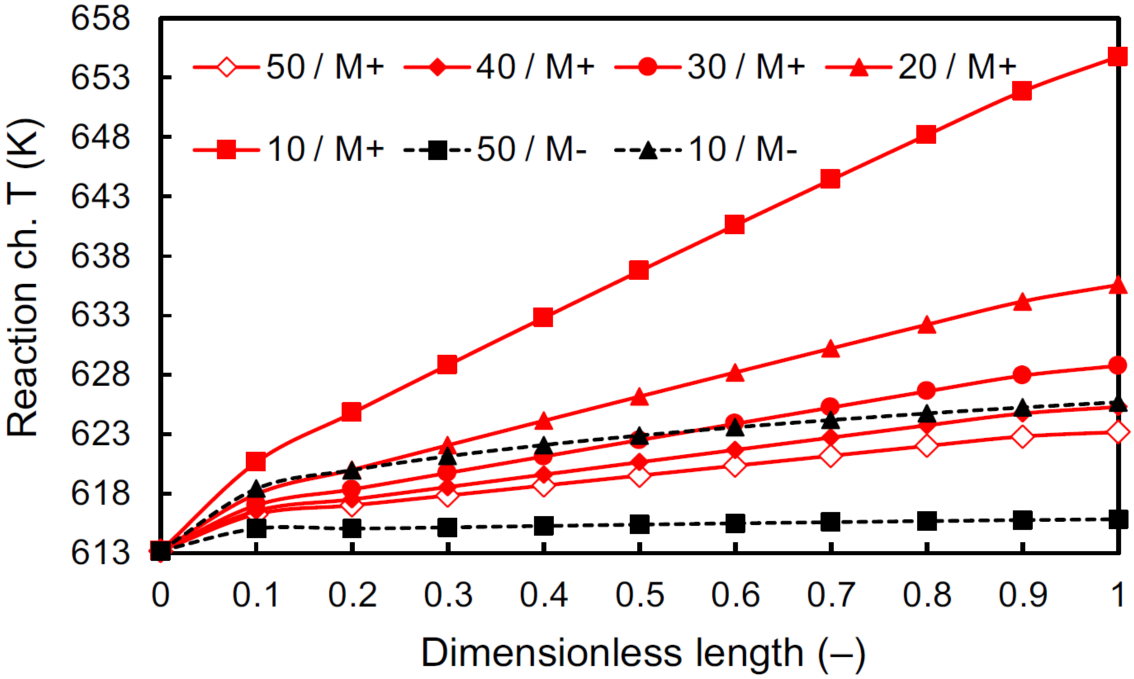

Figure 4.2. The effect of F_{in}^{p}/F_{in}^{R} on the reaction channel temperature (T_{in}^{R} = 613 K, p_{in}^{R} = 50 bar, ΔT_{in} = 0 K, space velocity = 1.5×10^{-3} m^3 kg_{cat}^{-1} s^{-1}, H_2/N_2 = 3).

One should note that the results obtained here favored the condition where the ratio of the inlet molar flow rate of the permeate channel was 50 times that of the inlet molar flow rate of the reaction channel. For different type of reactions or poor cooling capabilities, one might need higher or cooling numerical values for this ratio. The necessary amount must be determined according to the operating parameters and can not be considered independent of these parameters. One should carry out detailed simulations to obtain the necessary amount of the inlet molar flow rate of the permeate gas. Moreover, different type of coolant gas would lead to different results as the heat capacity of the gas would be different than the one employed here. Gas with higher heat capacity would be able to sweep away the heat generated by the reaction more effectively, resulting in lower temperatures along the reactor. However, it must also be economically feasible to employ such high flow of gas from engineering point of view, as the permeate channel gas inlet molar flow rate is usually much higher than the reaction channel gas inlet molar flow rate.

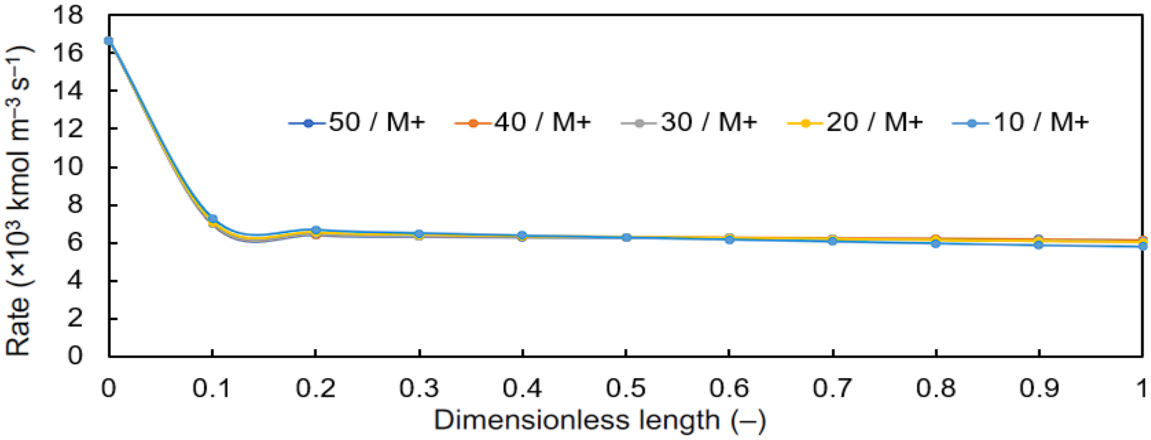

Figure 4.3. The effect of F_{in}^{p}/F_{in}^{R} on the rate profile along the (T_{in}^{R} = 613 K, p_{in}^{R} = 50 bar, ΔT_{in} = 0 K, space velocity = 1.5×10^{-3} m^3 kg$_{cat}^{-1}$ s^{-1}, H_2/N_2 = 3).

Table 4.1. The effect of F_{in}^{p}/F_{in}^{R} on nitrogen conversion.

Simulation	N_2 Conversion (%)
50 / M+	47.4
40 / M+	47.4
30 / M+	47.4
20 / M+	47.4
10 / M+	47.2

Table 4.2. The effect of F_{in}^{p}/F_{in}^{R} on the amount of NH_3 through the membrane.

Simulation	Total amount of ammonia that has passed through the membrane ($\frac{mol}{s} x\ 10^9$)
50 / M+	5.63
40 / M+	5.62
30 / M+	5.60
20 / M+	5.55
10 / M+	5.40

4.3. Effect of Changing Inlet Space Velocity

Feed gas inlet space velocity has been increased to capture the effect of space time changes in the reactor. The variation is done such that the default reactor conditions still prevailed by keeping inlet temperature of permeate and reaction gas at 613 K and 50 bar. Then, as the concentration at the inlets are the same, one can increase the molar flow rate by increasing the linear velocity at the reactor inlet in the simulation, since the cross-sectional area of the reactor is constant. Remember that in the default condition, inlet reactor volumetric flow rate was chosen to be 1.5 x 10^{-3} m^3 kg_{cat}^{-1} s^{-1}.

Below is the Figure 4.4 representing the cases in which default inlet reactor volumetric flow rate of 1.5 x 10^{-3} m^3 kg_{cat}^{-1} s^{-1} is compared with other inlet reactor volumetric flow rates of 3.0 x 10^{-3} m^3 kg_{cat}^{-1} s^{-1}, 4.5 x 10^{-3} m^3 kg_{cat}^{-1} s^{-1}, and 6 x 10^{-3} m^3 kg_{cat}^{-1} s^{-1}. One can easily observe the fact that the reason of choice of operating at default conditions lends itself in remarkably higher nitrogen conversion value that can be seen in Figure 4.4(b). A twofold increase in the inlet space velocity of feed gas at the same conditions leads to nigh-half drop in conversion over the default condition.

The reason why nitrogen conversion drops so drastically is that increasing feed gas inlet space velocity (or simply the inlet linear velocity, since these terms refer to the same results) reduces the exposure of reactant gases to the catalyst. This also holds true for the membrane as well, as faster flow of gases reduces the contact time of reactant gases on membrane. This fact can be observed when one examines the amount of ammonia that has passed through the membrane. However, we saw only about 7% drop in the molar flow rate of ammonia that has passed through the membrane when the space velocity is 6.0 x 10^{-3} m^3 kg_{cat}^{-1} s^{-1} compared to 1.5 x 10^{-3} m^3 kg_{cat}^{-1} s^{-1} (Table 4.3), which is due to the fact that ammonia in the permeate channel were already rather dilute even when the space velocity of feed gas is 1.5 x 10^{-3} m^3 kg_{cat}^{-1} s^{-1}. This means that low permeability is not the main factor responsible for the high drop in conversion. Reactant gas exposure to the catalyst is the key point.

Reducing inlet space velocity causes an additional effect. Outlet temperature increases as the inlet space velocity of feed gas is decreased. One expects this result since additional conversion of reactants stemming from higher exposure time of reactant gases to the catalyst and membrane causes more heat to be generated as the reaction is highly exothermic. Another additional effect is that slower flow of gases causes higher temperature gradients along the reactor as heat generated along the reactor is swept away slower.

One can choose a space velocity below 1.5 x 10^{-3} m^3 kg_{cat}^{-1} s^{-1} to attain higher conversion value. However, any value for the feed space velocity below 1.5 x 10^{-3} m^3 kg_{cat}^{-1} s^{-1} causes temperature increase problem, as 623 K threshold would definitely be exceeded (Figure 4.4(a)), posing a serious threat as to the life expectancy of the membrane. Moreover, the breakdown of thermodynamic limitations has already provided us with enormous efficiency over membraneless simulations. When membrane is integrated into the reactor with feed inlet space velocity of 1.5 x 10^{-3} m^3 kg_{cat}^{-1} s^{-1}, 47.4% nitrogen conversion is achieved. If no membrane is integrated with the same feed inlet space velocity, nitrogen conversion tops out at only 13.5%. For all space velocity operating points described here, integration of membrane causes intense amount of increase in nitrogen conversion compared to membraneless simulations, with the lowest increase being about 72% when the space velocity is 6.0 x 10^{-3} m^3 kg_{cat}^{-1} s^{-1}. Increase in nitrogen conversion becomes 250% when the space velocity is 1.5 x 10^{-3} m^3 kg_{cat}^{-1} s^{-1} due to aforementioned effects.

Although overall temperature gradients increase as expected when inlet space velocity is lowered (Figure 4.4(a)), a near-isothermal trend is observed in the front side of the reactor between dimensionless lengths of 0.1 and 0.2. This isothermal trend is due to the competing of mass transfer rate and reaction rate. When mass transfer rate is not fast enough at the beginning, ammonia that has been produced has not been transferred to the permeate channel yet, leading to a temporary halt in the reaction rate, rendering the reaction at equilibrium. However, when the mass transfer rate is sufficient enough, reaction rate begins to increase again due to suction of ammonia from the reaction channel, and we begin to see the temperature increasing again. In other words, when there is a membrane in the system that allows the mass transfer of a component, one is not only bound to how fast the reaction proceeds, but also the mass transfer rate of the specific components that pass through the membrane.

There is a hidden downside of decreasing inlet space velocity. Although higher nitrogen conversion values are achieved, due to less molar flow rate, overall converted amount of nitrogen or overall produced amount of ammonia drops. The gravity of choosing an appropriate value for inlet feed gas space velocity is evident from an engineering point of view. After all, an engineer has to choose a configuration such that the plant where he works makes better profit and the configuration returns the initial investment costs more quickly.

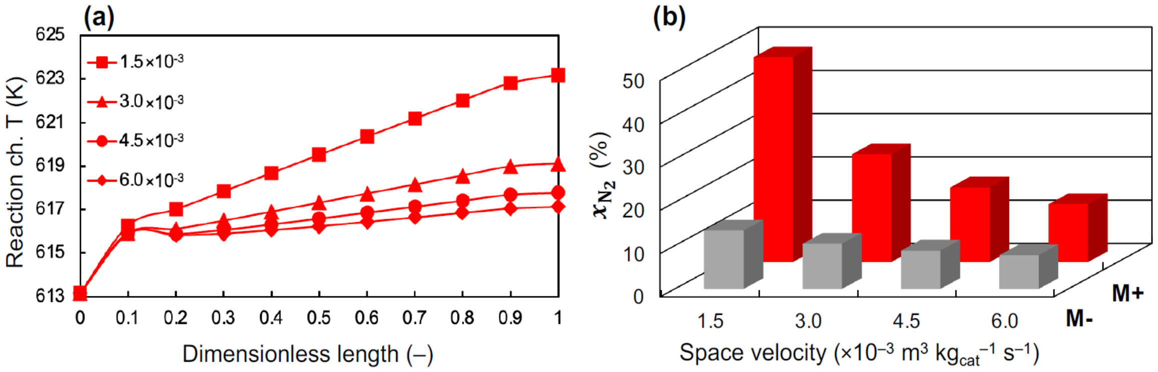

Figure 4.4. The effect of space velocity on the reaction channel temperature(a) and per cent N_2 conversion(b) ($T_{\mathrm{in}}^{\mathrm{R}}$ = 613 K, $p_{\mathrm{in}}^{\mathrm{R}}$ = 50 bar, ΔT_{in} = 0 K, H_2/N_2 = 3, $F_{\mathrm{in}}^{\mathrm{p}}/F_{\mathrm{in}}^{\mathrm{R}}$ = 50).

Table 4.3. The SV effect on the amount of NH_3 through the membrane.

Simulation	Total amount of ammonia that has passed through the membrane ($\frac{mol}{s} x\ 10^9$)
$1.5\mathrm{x}10^{-3}$	5.63
$3.0\mathrm{x}10^{-3}$	5.52
$4.5\mathrm{x}10^{-3}$	5.38
$6.0\mathrm{x}10^{-3}$	5.24

4.4. Effect of Changing Inlet Temperature

Feed gas inlet temperature is decreased by 10 K four times to see the effect of temperature on rate of reaction and the gravity of operating at temperature as high as possible. All the other operating conditions are chosen such that the feed gas inlet space velocity is 1.5×10^{-3} $m^3 \, kg_{cat}^{-1} \, s^{-1}$, feed gas and permeate gas pressure is 50 bar, the permeate gas inlet molar flow rate/feed gas inlet molar flow rate ratio is 50 (The permeate gas enters the permeate channel at 50 times higher velocity than the feed gas enters the reaction channel.), and the temperature difference between feed gas inlet and permeate gas inlet is 0 K. Decreasing the temperature means ideal gas concentrations are also changing. Consequently, inlet linear velocities of the feed gas permeate gas are changing.

Figure 4.5(c) shows that appreciable drop in conversion occurs for every 10 K temperature drop in each of simulations. This proves that the rate of reaction is highly dependent on temperature and one cannot operate at much lower temperatures than 583 K even when a membrane is integrated into the system since the single-pass conversion would approach a traditional Haber Bosch reactor conversion values, meaning that the advantage of the system is largely lost due to lower efficiency. High temperature is inevitable for this system.

There needs to be an imaginary membrane capable of much higher permeance of ammonia while being also selective. Then, one might be able to operate at much milder temperatures as the decrease in rate of reaction is compensated by the higher permeance of membrane. For this imaginary membrane, one must consider temperature limitations as well.

The system’s advantage is obvious. Rather high single-pass conversion value of 47.4% (Figure 4.5(c)) is achieved when the inlet temperatures of the feed gas and permeate gas is chosen to be 613 K. Compared to traditional Haber Bosch process, this is an enormous improvement.

Note that temperature increase along the reactor is proportional to conversion, as more conversion means more heat is generated due to exothermic nature of the reaction, as can be seen in Figure 4.5(a). However, 50 times faster inlet velocity of the permeate gas reduces the immense temperature increase by sweeping away the heat generated along the reactor, rendering the overall temperature increase between outlet and inlet at just 10 K for 613 K / M+ in Figure 4.5(a).

Note that operating at inlet temperature of 613 K has another advantage. It is the sole operating point for which thermodynamic limit was exceeded, as can be seen in Figure 4.5(c). However, all temperature operating points denoted here have already exhibited immense amount of improvement in nitrogen conversions. Moreover, integration of membrane also has a magnifying effect in that every 10 K increase in inlet temperature yields higher improvement in nitrogen conversion values compared to every 10 K increase in membraneless simulations (Figure 4.5(a) and Figure 4.5(c)). One is of course able to obtain higher conversion values when temperature is increased from 583 K to 613 K in membraneless simulations, with the increase in nitrogen conversion being about 37% higher (Figure 4.5(c)). However, the increase in conversion when membrane is integrated into the reactor and temperature is increased from 583 K to 613 K becomes nearly 73%, nearly double of the former value (Figure 4.5(c)).

The rather small gain in conversion when no membrane is present and temperature is increased in the configuration is due to the fact that the reaction is approaching thermodynamic equilibrium rapidly, as can be seen from the Figure representing rate profiles along the reactor in Figure 4.5(b). For 613 K / M- simulation, rate of reaction is higher generally than 583 K / M- simulations since temperature is higher. However, towards the end of the reactor, in these two simulations the rate of reactions are pretty much equal. Without a membrane, one cannot prevent the reaction from slowing down. Note that in 613 K / M+ and 583 K / M+ simulations in Figure 4.5(b), the reaction rates drop as well due to conversion of reactants to ammonia. However, the drop in the rate is much slower and the reaction is still capable of continuing to produce ammonia. Indeed, if the reactor had been longer, the increase in conversion would have still yielded promising results.

Figure 4.5(d) displays the outlet molar flow rates of ammonia. As the inlet temperature increases, more ammonia is produced. This holds true for all the simulations, whether membrane was integrated or not. However, it can be seen that 613 K / M+ is the most efficient configuration in another way, as the ammonia molar flow rate at the exit of the permeate channel is the highest. This happens due to the fact that higher inlet temperature causes the rate of reaction and the mass transfer rate to be higher, meaning that more ammonia is produced and it is possible to recover more of the ammonia in the permeate channel. The mass transfer rate is higher due to the fact that the partial pressure difference between the reaction channel and the permeate channel increases.

In summary, inlet temperature ought to be as high as possible in order to obtain the highest nitrogen conversion. However, it should also be within the safe operating points for the membrane.

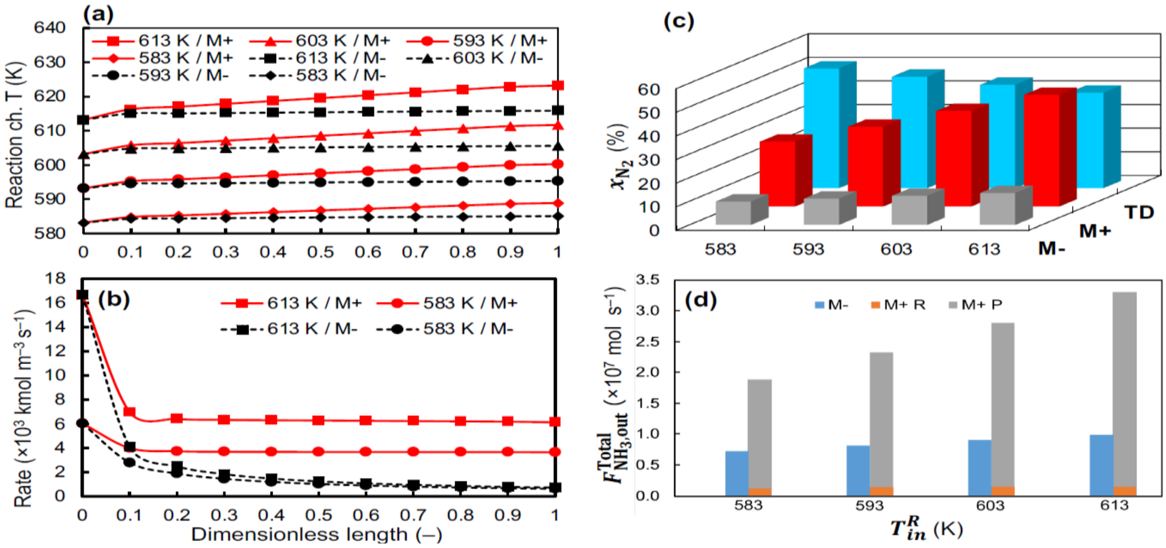

Figure 4.5. The effect of reaction channel inlet temperature on the reaction channel temperature(a), the reaction rate(b), per cent N_2 conversion(c) and NH_3 molar flow rate at the reactor exit(d). (p_{in}^{R} = 50 bar, ΔT_{in} = 0 K, H_2/N_2 = 3, space velocity = 1.5 ×10^{-3} m^3 kg_{cat}^{-1} s^{-1}, $F_{\text{in}}^{\text{p}}/F_{\text{in}}^{\text{R}}$ = 50).

4.5. Effect of Changing Pressure

The default pressure has been chosen to be 50 bar, at both feed and permeate gas inlets. Inlet temperatures are still 613 K at both permeate channel inlet and reaction channel inlet.

Inlet space velocity of the feed gas (STP) is 1.50 x 10^{-3} m^3 kg_{cat}^{-1} s^{-1} , and the permeate gas inlet molar flow rate/feed gas inlet molar flow rate ratio is 50. In this section, the inlet concentrations change due to ideal gas law. Pressure has a dramatic effect on nitrogen conversion for the reaction of nitrogen and hydrogen to produce ammonia. Reaction rate depends strongly on pressure alongside with temperature. Below is the Figure 4.6 displaying the runs in which pressure was 50 bar, 40 bar, and 30 bar. There is no pressure difference (ΔP) between permeate channel and reaction channel. This choice is justified as creating a pressure difference between permeate channel and reaction channel is dangerous as there will be a constant force the membrane has to endure over a very small region. If 5 bar of pressure difference is induced for the configuration, with the permeate channel inlet pressure being at 45 bar and the reaction channel inlet pressure being at 50 bar, 45 Newton upward force is created by the reaction channel acting upon the membrane for every repeating unit. If the permeate channel inlet pressure is adjusted to 40 bar, that upward force doubles in magnitude with 90 Newton, about the weight of 9 kg. Operating at constant pressure for both sides is safer since the membrane would not be exposed to force imbalance over a very small region.

Moreover, inducing a pressure difference between the reaction channel and permeate channel would not yield promising improvements, since the ammonia that has passed through the membrane is already rather diluted due to 50 times higher flow rate in the permeate channel. Partial pressure of ammonia is negligible and close to 0 bar in the permeate channel, so no significant amount of increase would be seen in the amount of ammonia that has passed through the membrane. If permeate gas inlet molar flow rate/feed gas inlet molar flow rate ratio were chosen to be less than 50, inducing a partial pressure difference between the channels could have been more effective, as the ammonia partial pressure in the permeate channel would be higher when there is no pressure difference between the channels due to the fact that ammonia that has passed through the membrane now would have been mixed with fewer amount of nitrogen gas, rendering its partial pressure higher in the permeate channel. Therefore, a possible solution would be inducing a partial pressure difference between the channels so that the ammonia partial pressure in the permeate channel is lowered to induce membrane to absorb more ammonia from the reaction channel.

Inducing pressure difference between the channels might have also proven to be effective if the membrane ammonia permeance were higher than 160 GPU.

The effect of pressure is evident. We saw nearly 10% decrease in nitrogen conversion for every 10 bar decrease in pressure, as can be seen in Figure 4.6(c). Consequently, the temperature increase alongside the reactor is less, as less heat is generated when less reactant is converted into product (Figure 4.6(a)).

Rate profiles along the reactor supports what has been just mentioned in Figure 4.5(b). Pressure, alongside with temperature, is an important parameter, yielding higher rate values along the reactor as it is chosen to be higher. Note that in Figure 4.6(b) the rate values for 50 bar / M- and 30 bar / M- were very close to equilibrium towards the end of the reactor, while the drop in rate values were much slower due to the presence of membrane. Indeed, we could have seen the reaction proceeding to higher conversion of nitrogen, had the channels been longer. The presence of membrane allows one to break down thermodynamic limits, thereby making it possible to achieve rather high conversion levels.

Figure 4.6(d) shows the ammonia flow rates at the exit. Note that in 50 bar the permeate channel ammonia molar flow rate is the highest. The explanation is given in Section 4.4. In short, increase in pressure causes more ammonia to be produced and also causes more ammonia to pass through the membrane to permeate channel, as the increase in pressure increases both the rate of reaction and the mass transfer rate. The mass transfer rate increase is due to two effects. The flux of mass is affected by the total operating pressure as can be seen in Equation (3.1) and Equation (3.3). Moreover, due to the increase in the rate of reaction, a small additional positive effect in terms of the mass transfer occurs (More ammonia is accumulated in reaction channel, leading to higher driving force for the mass transfer).

One should note that as pressure increases, operating cost would also increase. However, the default simulation pressure 50 bar is still significantly less than traditional operating pressures of Haber-Bosch process.

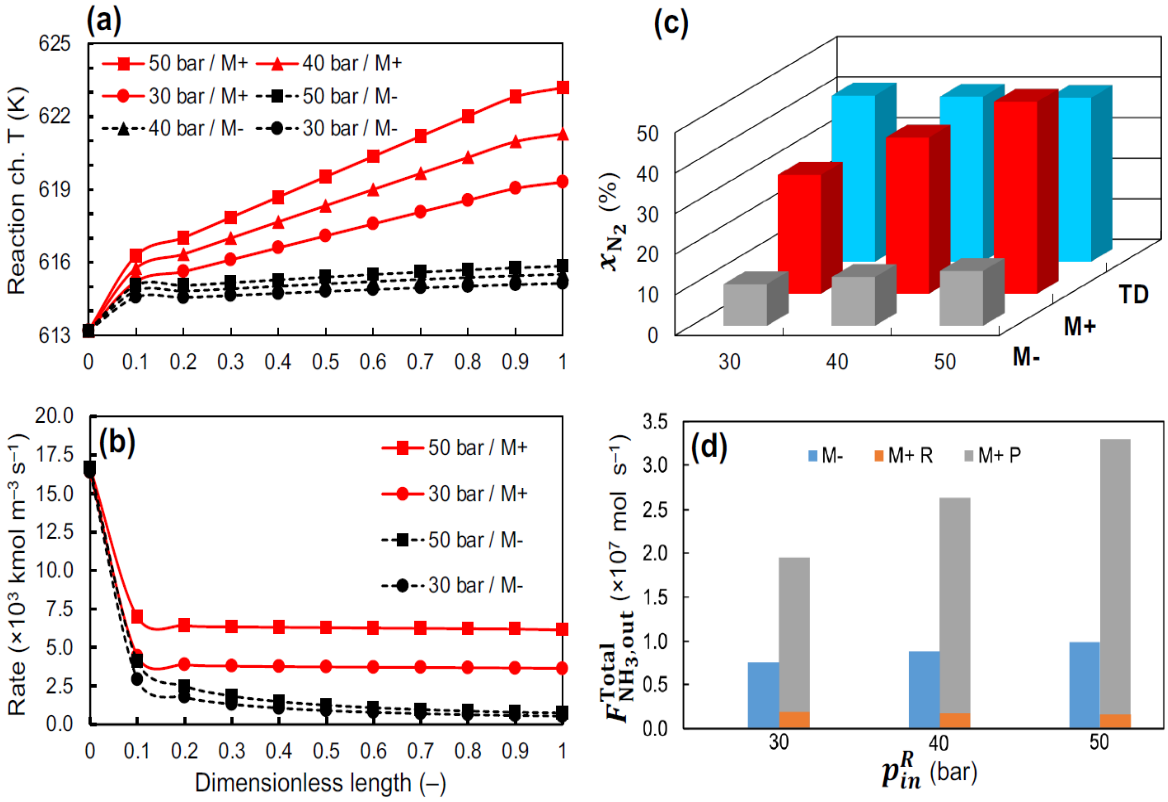

Figure 4.6. The effect of reaction channel inlet pressure the reaction channel temperature(a), the reaction rate(b), per cent N_2 conversion(c) and NH_3 molar flow rate at the reactor exit(d). (T_{in}^{R} = 613 K, ΔT_{in} = 0 K, H_2/N_2 = 3, space velocity = 1.5 ×10^{-3} m^3 kg_{cat}^{-1} s^{-1}, $F_{\text{in}}^{\text{p}}/F_{\text{in}}^{\text{R}}$ = 50).

4.6. Effect of Changing Temperature Difference

Permeate gas inlet temperature is varied while keeping the feed gas inlet temperature at 613 K. At both side inlets, pressure is still 50 bar. Inlet feed volumetric flow rate per kg of catalyst is still 1.50 x 10^{-3} m^3 kg_{cat}^{-1} s^{-1}. Moreover, the molar flow rate of the inlet permeate gas is still 50 times that of the feed gas. As the temperature at the inlet of permeate gas changes, concentration at that inlet changes, just as in Section 4.5. However, this time, according to ideal gas law, the concentration difference between the inlets is rather small compared to cases in which pressure changed since 10 or 20 K decrease in temperature does not change the concentration significantly. However, a small adjustment was still made in permeate gas inlet velocities but the ratio does not deviate much from 50.

Below is the Figure 4.7 displaying the temperature and nitrogen conversion for default case (ΔT=0 K), ΔT=10 K case and ΔT=20 K case. Note that temperature profiles for $\Delta T \neq 0$ cases do not follow a monotonic temperature increase along the reactor this time. Near the inlet of the reaction channel, there is a sudden drop in temperature, which is due to the rapid cooling of the reaction channel content as the permeate gas temperature is cooler now. After that point, the heat generated due to exothermic reaction becomes more intensified as the permeate gas is now unable to cool the reaction channel content anymore. As conversion continues to increase, the monotonic temperature increase along the reactor is seen again. Note that when ΔT=20, temperature at the end of the reaction channel is lowest since the sudden drop temperature was also the lowest for this case.

Inducing a temperature difference ΔT between the reaction channel inlet and permeate channel inlet might be necessary for cases in which the reaction is rather exothermic or the membrane structure is not durable enough for high operating temperature. Then, one can easily adjust the temperature in permeate channel so that temperature increase is hindered. The cost of temperature decrease is evident. As more temperature difference ΔT is induced between the reaction channel inlet and permeate channel inlet, the average rate of reaction along the entire reactor also drops, leading to lower conversion values. In our simulations, even a moderate temperature difference of ΔT=10 K caused nearly 11.5% in nitrogen conversion.

The default case is more profitable between these three cases below as the temperature increase in the default case does not cause extreme temperature increase and a problem for the safety of $ZnCl_2$-IMS membrane. A different type of membrane that is less durable would cause a performance loss for the system of interest, as then one might be forced to employ a configuration in which the temperature difference between the feed gas inlet and the sweep gas inlet is not 0. This configuration, as discussed, causes the reaction to significantly underperform, as the reaction rate tends to be the fastest towards the inlet region of the reactor.

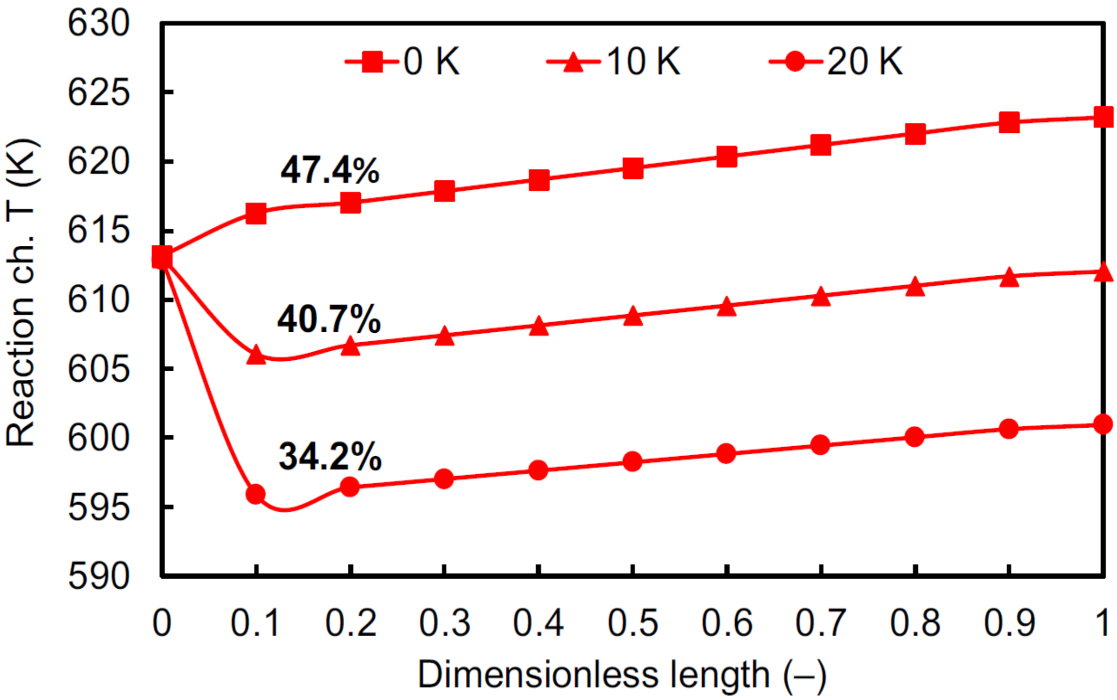

Figure 4.7. Temperature profiles along the reaction channel obtained at ΔT_{in} values of 0, 10 and 20 K ($T_{\mathrm{in}}^{\mathrm{R}}$ = 613 K, $p_{\mathrm{in}}^{\mathrm{R}}$ = 50 bar, H_2/N_2 = 3, space velocity = 1.5 ×10^{-3} m^3 kg_{cat}^{-1} s^{-1}, $F_{\mathrm{in}}^{\mathrm{p}}/F_{\mathrm{in}}^{\mathrm{R}}$ = 50).

4.7. Effect of Changing H_2/N_2 ratio in the Reaction Gas

So far, all the simulations we have discussed employed reactor feed inlet H_2/N_2 ratio as 3. The choice is justified as it is the stoichiometric ratio of the reaction occurring inside the reactor. To find out how nitrogen conversion is affected by varying this ratio, two more additional runs have been simulated in which feed inlet H_2/N_2 ratio was 2 and 4. These runs were still based on the default case, so the only change is the feed inlet ratio, with inlet molar flow rates remain unchanged. At both feed and permeate gas inlets, pressure is still 50 bar. Inlet feed volumetric flow rate per kg of catalyst is still 1.50 x 10^{-3} m^3 kg_{cat}^{-1} s^{-1} . Moreover, the inlet molar flow rate of the permeate gas is still 50 times that of the feed gas. There is no pressure difference or temperature difference between reaction channel and permeate channel.

This time, the metric to keep track of is not the nitrogen conversion, as it is misleading in that the nitrogen amount itself at the reactor inlet is changing. Therefore, the converted amount of nitrogen is observed, see Figure 4.8(c).

It is obvious that the rate of reaction is changing by only modifying the H_2:N_2, as can be seen in Figure 4.8(b). As the hydrogen per cent in the feed increases, the total converted amount of nitrogen increases (Figure 4.8(c)). Therefore, highest amount of ammonia is produced when H_2/N_2 ratio is set to be 2, which is lower than the stoichiometric number (Figure 4.8(c)).

The trend in reaction temperature follows the converted amount of ammonia, as can be seen in Figure 4.8(a). As more nitrogen is converted, more heat is generated inside the reaction channel, leading to higher outlet temperatures. However, the differences between outlet temperatures are small. Even smaller are the temperature profiles when membrane is disabled, as the rate of reaction is already rather low to be influenced in a noticeable extent by varying H_2/N_2 ratio. The reaction is essentially in equilibrium towards the end of the channels for membraneless runs.

The molar flow rate of ammonia at the exit can be seen in in Figure 4.8(d). Note that more ammonia is produced and more of it passed through the membrane to permeate channel in $H_2/N_2 = 2$, due to the rate of reaction being higher when the inlet H_2/N_2 is lower.

Choosing the H_2/N_2 ratio in the reactor inlet to be 2 would be a justifiable choice if the membrane implemented in this study were more durable to temperatures above 623 K. The ratio is therefore deliberately chosen to be 3 by default. Another characteristic of this ratio is that it happens to be the stoichiometric ratio of the reactants. However, one should also take into the account the availability of the inlet gases. After all, sources of inlet hydrogen and nitrogen and the availability of these sources are important factors in setting up a plant where this configuration is employed. In other words, an engineer should implement careful designation methods to make sure the constant, clean, and profitable supply of the reactant components. In that way, we hereby could ensure that the proposed process would be much more efficient, as it would depend on other green technologies that supply the reactants of ammonia.

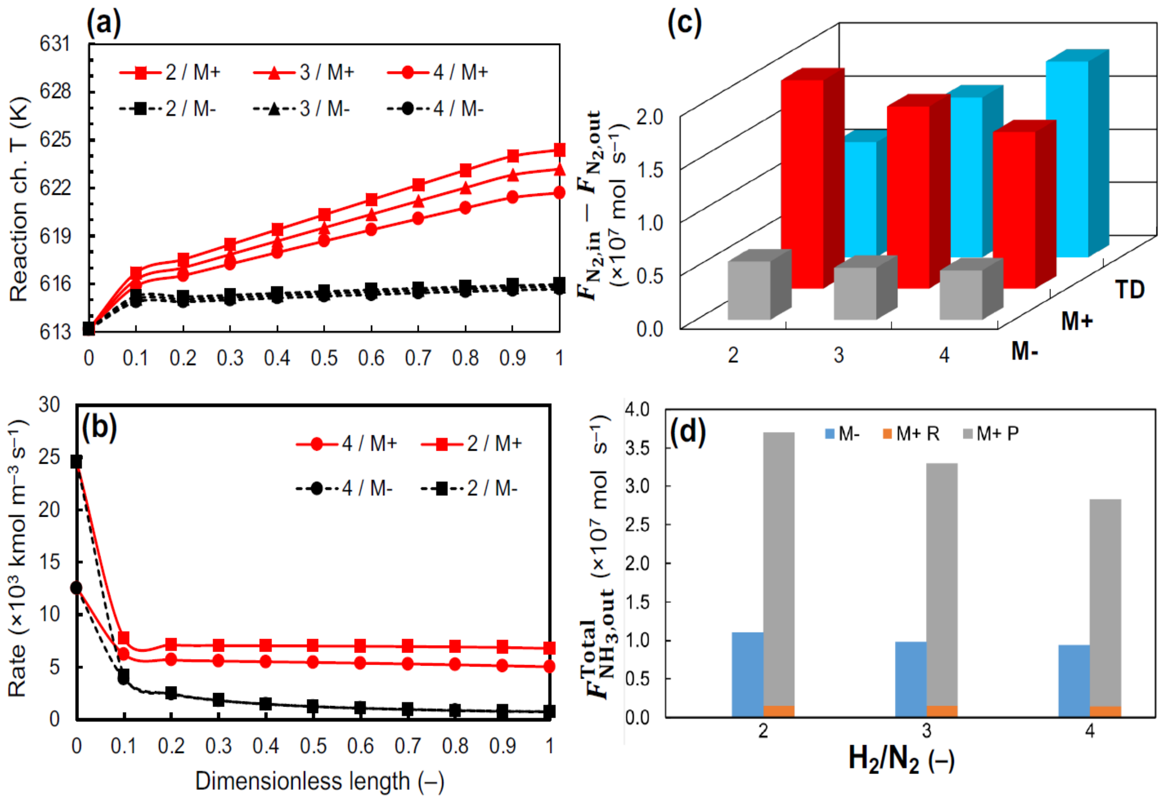

Figure 4.8. The effect of molar inlet H_2/N_2 ratio on the reaction channel temperature(a), the reaction rate(b), molar flow rate of the converted N_2(c) and NH_3 molar flow rate at the reactor exit(d). (T_{in}^{R} = 613 K, p_{in}^{R} = 50 bar, ΔT_{in} = 0 K, space velocity = 1.5×10^{-3} m^3 kg_{cat}^{-1} s^{-1}, F_{in}^{p}/F_{in}^{R} = 50).

5. CONCLUSION

The advantage of production of ammonia in a wall-coated membrane microchannel reactor is shown. Small-scale production of ammonia could be profitable and much more efficient with this configuration. In operating conditions much milder than that of the Haber-Bosch process, much higher single-pass nitrogen conversion could be obtained. The effect of several parameters on nitrogen conversion and reactor temperature is displayed in this report.

Inlet temperature is important in that higher inlet temperature of reaction gas results in higher nitrogen conversion and magnifies the effect of membrane. However, the durability of membrane is important and a restrictive factor for the choice of inlet temperature.

Pressure is also important in that higher operating pressure results in higher nitrogen conversion. The choice of operating pressure is restricted by the profitability, and the temperature limitation of the membrane.

Inducing a temperature difference between permeate channel and the reaction channel could be beneficial with regard to the safety of the membrane. If the permeate gas is colder, the temperature can be reduced. The cost is nitrogen conversion, and therefore profitability.

Inlet space velocity is also a dominant factor with regard to the enhancement of membrane integration. When the space velocity is lower, the flowing gas has more time to contact with both the catalyst and the membrane, therefore increasing the mass transfer rate of the membrane and also the reaction rate, a positive effect for both factor. The choice of inlet space velocity is restricted by the fact that although the process becomes more efficient in terms of nitrogen conversion, the amount of ammonia produced decreases. Therefore, one has to have more of the repeated units inside multichannel reactor block, thereby increasing the capital cost and the volume required for sufficient production.

Permeate gas inlet molar flow rate is an important factor in terms of diluting the ammonia that has passed through membrane to permeate channel. However, in this configuration, ammonia has been found to already have been sufficiently diluted even when the ratio of inlet gas molar flow rate of the permeate channel to reaction channel was 20. Further enhancement to that ratio did not yield sufficient benefits in terms of nitrogen conversion. However, as permeate gas inlet molar flow rate increases, the temperature increase is also restricted. Therefore one has to choose a ratio such that the safe of membrane is ensured. The increase in permeate gas inlet molar flow rate also comes with the downside that operating cost increases.

H_2:N_2 ratio in the feed is a strong factor compared to the others. It is influenced by the rate of reaction. With this configuration, it was found that H_2:N_2 should be as low as possible to achieve highest amount of ammonia production.

5.1. Recommendations

It was obvious that the presence of membrane caused the ammonia production to be much more efficient than the Haber-Bosch process. The membrane permeability for ammonia is 160 GPU herein. A higher GPU value would lead to higher mass transfer rates for the ammonia, which would enhance the rate of reaction and therefore ammonia production even further.

The limitation of operating temperature is the restrictive factor why a higher nitrogen could not have been achieved. As the studies for membrane go on, with the invention of more capable and more durable membranes, higher operating temperature could be achieved without causing damage to the structure of the membrane, thereby making it possible to achieve conversion values much higher than ~50%.

A more active catalyst would be the process to be more efficient, as the rate of reaction would increase. Therefore, it would be possible to achieve conversion values much higher than ~50% if a more active catalyst was used.

REFERENCES

1. Victor, D. [The New York Times], “World Population Reaches 8 Billion, UN Says”, 2022, https://www.nytimes.com/2022/11/15/world/world-population-8-billion.html, accessed on May 06, 2023.
2. European Environment Agency, “A Future Based on Renewable Energy”, 2022. https://www.eea.europa.eu/signals/signals-2022/articles/a-future-based-on-renewable-energy, accessed on May 06, 2023.
3. O’Malley, I. [AP News], “U.S. Renewable Electricity Surpassed Coal in 2022”, 2023, https://apnews.com/article/renewable-energy-coal-nuclear-climate-change-dd4a0b168fe057f430e37398615155a0 , accessed on May 06, 2023.
4. BP, “Statistical Review of World Energy 2022”, https://www.bp.com/content/dam/bp/business-sites/en/global/corporate/pdfs/energy-economics/statistical-review/bp-stats-review-2022-full-report.pdf, accessed on May 06, 2023.
5. The Economist, “Deadly, Dirty, Indispensable: the Nitrogen Industry Has Changed the World”, 2022, https://www.economist.com/christmasspecials/2022/12/20/deadly--dirty-indispensable-the-nitrogen-industry-has-changed-the-world , accessed on May 07, 2023.
6. Britannica, “Haber-Bosch Process”, https://www.britannica.com/technology/Haber-Bosch-process, accessed on May 07, 2023.
7. Dincer, I., D. Erdemir, M. I. Aydin, H. Karasu, and G. Vezina, *Ammonia Energy Technologies*, Springer, Cham, 2022.
8. Baltrusaitis, J., “Sustainable Ammonia Production,” *ACS Sustainable Chemistry & Engineering*, Vol. 5, No. 11, p. 9527, 2017.
9. Patil, B. S., Q. Wang, V. Hessel, and J. Lang, “Plasma N_2-Fixation: 1900–2014”, *Catalysis Today*, Vol. 256, pp. 49–66, 2015.

10. Erisman, J. W., M. A. Sutton, J. Galloway, Z. Klimont, and W. Winiwarter, “How a Century of Ammonia Synthesis Changed the World”, *Nature Geoscience*, Vol. 1, No. 10, pp. 636–639, 2008.

11. Pattabathula V., J. Richardson [AIChE], “Introduction to Ammonia Production”, 2016, https://www.aiche.org/resources/publications/cep/2016/september/introduction-ammonia-production , accessed on Jun. 13, 2023.

12. Lin, B., T. Wiesner, and M. Malmali, “Performance of a Small-Scale Haber Process: A Techno-Economic Analysis”, *ACS Sustainable Chemistry & Engineering*, Vol. 8, No. 41, pp. 15517–15531, 2020.

13. Giddey, S., S. P. S. Badwal, and A. Kulkarni, “Review of Electrochemical Ammonia Production Technologies and Materials”, *International Journal of Hydrogen Energy*, Vol. 38, No. 34, pp. 14576–14594, 2013.

14. Appl, M., *Ammonia: Principles and Industrial Practice*, Wiley, Weinheim, 1999.

15. Appl, M., “Ammonia, 2. Production Processes”, *Ullmann’s Encyclopedia of Industrial Chemistry*, Wiley-VCH, Weinheim, 2011.

16. Rouwenhorst, K. H. R., A. G. J. Van der Ham, and L. Lefferts, “Beyond Haber-Bosch: The renaissance of the Claude process”, *International Journal of Hydrogen Energy*, Vol. 46, No. 41, pp. 21566–21579, 2021.

17. Hellman, A., K. Honkala, S. Dahl, C. H. Christensen, and J. K. Nørskov, “Ammonia Synthesis: State of the Bellwether Reaction”, *Comprehensive Inorganic Chemistry II: From Elements to Applications*, Vol. 7, pp. 459–474, 2013.

18. Khademi, M. H. and R. S. Sabbaghi, “Comparison Between Three Types of Ammonia Synthesis Reactor Configurations in terms of Cooling Methods”, *Chemical Engineering Research and Design*, Vol. 128, pp. 306–317, 2017.

19. Humphreys, J., R. Lan, and S. Tao, “Development and Recent Progress on Ammonia Synthesis Catalysts for Haber–Bosch Process”, *Advanced Energy and Sustainability Research*, Vol. 2, No. 1, p. 2000043, 2021.

20. Han, W., S. Huang, T. Cheng, H. Tang, Y. Li, and H. Liu, "Promotion of Nb_2O_5 on the Wustite-Based Iron Catalyst for Ammonia Synthesis", *Applied Surface Science*, Vol. 353, pp. 17–23, 2015.

21. Yu, X., B. Lin, J. Lin, R. Wang, and K. Wei, "A Novel Fused Iron Catalyst for Ammonia Synthesis Promoted with Rare Earth Gangue", *Journal of Rare Earths*, Vol. 26, No. 5, pp. 711–716, 2008.

22. Raróg-Pilecka, W., A. Jedynak-Koczuk, J. Petryk, E. Miśkiewicz, S. Jodzis, Z. Kaszkur, and Z. Kowalczyk, "Carbon-Supported Cobalt–Iron Catalysts for Ammonia Synthesis", *Applied Catalysis A: General*, Vol. 300, No. 2, pp. 181–185, 2006.

23. Jafari, A., A. Ebadi, and S. Sahebdelfar, "Effect of Iron Oxide Precursor on the Properties and Ammonia Synthesis Activity of Fused Iron Catalysts", *Reaction Kinetics, Mechanisms and Catalysis*, Vol. 126, No. 1, pp. 307–325, 2019.

24. Taylor, D. W., P. J. Smith, D. A. Dowden, C. Kemball, and D. A. Whan, "Ammonia Synthesis and Related Reactions over Iron-Cobalt and Iron-Nickel Alloy Catalysts. Part I. Catalysts Reduced at 853 K", *Applied Catalysis*, Vol. 3, No. 2, pp. 161–176, 1982.

25. Baiker, A., R. Schloğl, E. Armbruster, and H. J. Güntherodt, "Ammonia Synthesis over Supported Iron Catalyst Prepared from Amorphous Iron-Zirconium Precursor: I. Bulk Structural and Surface Chemical Changes of Precursor during its Transition to the Active Catalyst", *Journal of Catalysis*, Vol. 107, No. 1, pp. 221–231, 1987.

26. Wang, P., H. Xie, J. Guo, Z. Zhao, X. Kong, W. Gao, F. Chang, T. He, G. Wu, M. Chen, L. Jiang, and P. Chen, "The Formation of Surface Lithium-Iron Ternary Hydride and its Function on Catalytic Ammonia Synthesis at Low Temperatures", *Angewandte Chemie International Edition*, Vol. 56, No. 30, pp. 8716–8720, 2017.

27. Kitano, M., J. Kujirai, K. Ogasawara, S. Matsuishi, T. Tada, H. Abe, Y. Niwa, and H. Hosono, "Low-Temperature Synthesis of Perovskite Oxynitride-Hydrides as Ammonia Synthesis Catalysts", *Journal of the American Chemical Society*, Vol. 141, No. 51, pp. 20344–20353, 2019.

28. Murakami, K., Y. Tanaka, R. Sakai, K. Toko, K. Ito, A. Ishikawa, T. Higo, T. Yabe, S. Ogo, M. Ikeda, H. Tsuneki, H. Nakai, and Y. Sekine, "The Important Role of N_2H

Formation Energy for Low-Temperature Ammonia Synthesis in an Electric Field", *Catalysis Today*, Vol. 351, pp. 119–124, 2020.

29. Fan, H., X. Huang, K. Kähler, J. Folke, F. Girgsdies, D. Teschner, Y. Ding, K. Hermann, R. Schlögl, and E. Frei, "In-Situ Formation of Fe Nanoparticles from FeOOH Nanosheets on γ-Al_2O_3 as Efficient Catalysts for Ammonia Synthesis", *ACS Sustainable Chemistry & Engineering*, Vol. 5, No. 11, pp. 10900–10909, 2017.

30. Yan, P., W. Guo, Z. Liang, W. Meng, Z. Yhin, S. Li, M. Li, M. Zhang, J. Yan, D. Xiao, R. Zou, and D. Ma, "Highly Efficient K-Fe/C Catalysts Derived from Metal-Organic Frameworks towards Ammonia Synthesis", *Nano Research*, Vol. 12, No. 9, pp. 2341–2347, 2019.

31. Czekajło Ł. and Z. Lendzion-Bieluń, "Wustite Based Iron-Cobalt Catalyst for Ammonia Synthesis", *Catalysis Today*, Vol. 286, pp. 114–117, 2017.

32. Tang, Y., Y. Kobayashi, N. Masuda, Y. Uchida, H. Okamoto, T. Kageyama, S. Hosokawa, F. Loyer, K. Mitsuhara, K. Yamanaka, Y. Tamenori, C. Tassel, T. Yamamoto, T. Tanaka, and H. Kageyama, "Metal-Dependent Support Effects of Oxyhydride-Supported Ru, Fe, Co Catalysts for Ammonia Synthesis", *Advanced Energy Materials*, Vol. 8, No. 36, p. 1801772, 2018.

33. Ye, T. N., S. W. Park, Y. Lu, J. Li, M. Sasase, M. Kitano, T. Tada, and H. Hosono, "Vacancy-Enabled N_2 Activation for Ammonia Synthesis on a Ni-Loaded Catalyst", *Nature*, Vol. 583, No. 7816, pp. 391–395, 2020.

34. Kojima R. and K. I. Aika, "Cobalt Molybdenum Bimetallic Nitride Catalysts for Ammonia Synthesis: Part 2. Kinetic Study", *Applied Catalysis A: General*, Vol. 218, No. 1–2, pp. 121–128, 2001.

35. Bion, N., F. Can, J. Cook, J. S. J. Hargreaves, A. L. Hector, W. Levason, A. R. McFarlane, M. Richard, and K. Sardar, "The Role of Preparation Route upon the Ambient Pressure Ammonia Synthesis Activity of Ni_2Mo_3N", *Applied Catalysis A: General*, Vol. 504, pp. 44–50, 2015.

36. Ye, T. N., S. W. Park, Y. Lu, J. Li, M. Sasase, M. Kitano, and H. Hosono, "Contribution of Nitrogen Vacancies to Ammonia Synthesis over Metal Nitride

Catalysts", *Journal of the American Chemical Society*, Vol. 142, No. 33, pp. 14374–14383, 2020.

37. Humphreys, J., R. Lan, D. Du, W. Xu, and S. Tao, "Promotion Effect of Proton-Conducting Oxide $BaZr_{0.1}Ce_{0.7}Y_{0.2}O_{3-\delta}$ on the Catalytic Activity of Ni towards Ammonia Synthesis from Hydrogen and Nitrogen", *International Journal of Hydrogen Energy*, Vol. 43, No. 37, pp. 17726–17736, 2018.

38. Narasimharao, K., P. Seetharamulu, K. S. Rama Rao, and S. N. Basahel, "Carbon Covered Mg–Al Hydrotalcite Supported Nanosized Ru Catalysts for Ammonia Synthesis", *Journal of Molecular Catalysis A: Chemical*, Vol. 411, pp. 157–166, 2016.

39. Wildfire, C., V. Abdelsayed, D. Shekhawat, R. A. Dagle, S. D. Davidson, and J. Hu, "Microwave-Assisted Ammonia Synthesis over Ru/MgO Catalysts at Ambient Pressure", *Catalysis Today*, Vol. 365, pp. 103–110, 2021.

40. Hattori, M., S. Iijima, T. Nakao, H. Hosono, and M. Hara, "Solid Solution For Catalytic Ammonia Synthesis from Nitrogen and Hydrogen Gases at 50 °C", *Nature Communications*, Vol. 11, No. 1, pp. 1–8, 2020.

41. Hattori, M., T. Mori, T. Arai, Y. Inoue, M. Sasase, T. Tada, M. Kitano, T. Yokoyama, M. Hara, and H. Hosono, "Enhanced Catalytic Ammonia Synthesis with Transformed BaO", *ACS Catalysis*, Vol. 8, No. 12, pp. 10977–10984, 2018.

42. Li, J., M. Kitano, T. N. Ye, M. Sasase, T. Yokoyama, and H. Hosono, "Chlorine-Tolerant Ruthenium Catalyst Derived Using the Unique Anion-Exchange Properties of $12\,CaO{\cdot}7\,Al_2O_3$ for Ammonia Synthesis", *ChemCatChem*, Vol. 9, No. 15, pp. 3078–3083, 2017.

43. Qiu, J. Z., J. Hu, J. Lan, L. F. Wang, G. Fu, R. Xiao, B. Ge, and J. Jiang, "Pure Siliceous Zeolite-Supported Ru Single-Atom Active Sites for Ammonia Synthesis", *Chemistry of Materials*, Vol. 31, No. 22, pp. 9413–9421, 2019.

44. Li, W., P. Liu, R. Niu, J. Li, and S. Wang, "Influence of CeO2 Supports Prepared with Different Precipitants over Ru/CeO_2 Catalysts for Ammonia Synthesis", *Solid State Sciences*, Vol. 99, p. 105983, 2020.

45. Inoue, Y., M. Kitano, M. Tokunari, T. Taniguchi, K. Ooya, H. Abe, Y. Niwa, M. Sasase, M. Hara, and H. Hosono, “Direct Activation of Cobalt Catalyst by $12CaO \cdot 7Al_2O_3$ Electride for Ammonia Synthesis”, *ACS Catalysis*, Vol. 9, No. 3, pp. 1670–1679, 2019.

46. Tarka, A., M. Zybert, E. Truszkiewicz, B. Mierzwa, L. Kępiński, D. Moszyński, and W. Rarõg-Pilecka, “Effect of a Barium Promoter on the Stability and Activity of Carbon-Supported Cobalt Catalysts for Ammonia Synthesis”, *ChemCatChem*, Vol. 7, No. 18, pp. 2836–2839, 2015.

47. Temkin, M. I. and V. Pyzhev, “Kinetics of ammonia synthesis on Promoted Iron Catalysts”, *Acta Physicochimica U.R.S.S.*, Vol. 12, pp. 327–356, 1940.

48. Nielsen, A., J. Kjaer, and B. Hansen, “Rate equation and Mechanism of Ammonia Synthesis at Industrial Conditions”, *Journal of Catalysis*, Vol. 3, No. 1, pp. 68–79, 1964.

49. Temkin, M. I., “Kinetics of Ammonia Synthesis under High Pressures”, *Zhurnal Fizicheskoi Khimii*, Vol. 24, pp. 1312-1325, 1950.

50. Imamura, K., S. Miyahara, Y. Kawano, K. Sato, Y. Nakasaka, and K. Nagaoka, “Kinetics of Ammonia Synthesis over Ru/Pr_2O_3”, *Journal of the Taiwan Institute of Chemical Engineers*, Vol. 105, pp. 50–56, 2019.

51. Sehested, J., C. J. H. Jacobsen, E. Törnqvist, S. Rokni, and P. Stoltze, “Ammonia Synthesis over a Multipromoted Iron Catalyst: Extended Set of Activity Measurements, Microkinetic Model, and Hydrogen Inhibition”, *Journal of Catalysis*, Vol. 188, No. 1, pp. 83–89, 1999.

52. Zhang, Z., J. D. Way, and C. A. Wolden, “Design and Operational Considerations of Catalytic Membrane Reactors for Ammonia Synthesis”, *AIChE Journal*, Vol. 67, No. 8, p. 17259, 2021.

53. Shen, H., C. Choi, J. Masa, X. Li, J. Qiu, Y. Jung, and Z. Shun, “Electrochemical Ammonia Synthesis: Mechanistic Understanding and Catalyst design”, *Chem*, Vol. 7, No. 7, pp. 1708–1754, 2021.

54. Rapson, T. D., C. M. Gregg, R. S. Allen, H. K. Ju, C. M. Doherty, X. Mulet, S. Giddey, and C. C. Wood, "Insights into Nitrogenase Bioelectrocatalysis for Green Ammonia Production", *ChemSusChem*, Vol. 13, No. 18, pp. 4856–4865, 2020.

55. Hinnemann, B. and J. K. Nørskov, "Catalysis by Enzymes: The Biological Ammonia Synthesis", *Topics in Catalysis*, Vol. 37, No. 1, pp. 55–70, 2006.

56. Nikačević, N., M. Jovanović, and M. Petkovska, "Enhanced Ammonia Synthesis in Multifunctional Reactor with in situ Adsorption", *Chemical Engineering Research and Design*, Vol. 89, No. 4, pp. 398–404, 2011.

57. Fogler, H. S., *Elements of Chemical Reaction Engineering*, Fifth Edition, Pearson, Iowa, 2016.

58. Wei, Q., J. M. Lucero, J. M. Crawford, J. D. Way, C. A. Wolden, and M. A. Carreon, "Ammonia Separation from N_2 and H_2 over LTA Zeolitic Imidazolate Framework Membranes", *Journal of Membrane Science*, Vol. 623, p. 119078, 2021.

59. Bhown A. and E. L. Cussler, "Mechanism for Selective Ammonia Transport through Poly(Vinylammonium Thiocyanate) Membranes", *Journal of the American Chemical Society*, Vol. 113, No. 3, pp. 742–749, 1991.

60. He Y. and E. L. Cussler, "Ammonia Permeabilities of Perfluorosulfonic Membranes in Various Ionic Forms", *Journal of Membrane Science*, Vol. 68, No. 1–2, pp. 43–52, 1992.

61. Kanezashi, M., A. Yamamoto, T. Yoshioka, and T. Tsuru, "Characteristics of Ammonia Permeation through Porous Silica Membranes", *AIChE Journal*, Vol. 56, No. 5, pp. 1204–1212, 2010.

62. Laciak, D. V., G. P. Pez, and P. M. Burban, "Molten Salt Facilitated Transport Membranes. Part 2. Separation of Ammonia from Nitrogen and Hydrogen at High Temperatures", *Journal of Membrane Science*, Vol. 65, No. 1–2, pp. 31–38, 1992.

63. Uriz, I., G. Arzamendi, E. López, J. Llorca, and L. M. Gandía, "Computational Fluid Dynamics Simulation of Ethanol Steam Reforming in Catalytic Wall Microchannels", *Chemical Engineering Journal*, Vol. 167, No. 2–3, pp. 603–609, 2011.

64. Hagen, S., R. Barfod, R. Fehrmann, C. J. H. Jacobsen, H. T. Teunissen, and I. Chorkendorff, “Ammonia Synthesis with Barium-Promoted Iron–Cobalt Alloys Supported on Carbon”, *Journal of Catalysis*, Vol. 214, No. 2, pp. 327–335, 2003.

65. Satterfield, C. N. and P. J. Cadle, “Gaseous Diffusion and Flow in Commercial Catalysts at Pressure Levels Above Atmospheric”, *Industrial and Engineering Chemistry Fundamentals*, Vol. 7, No. 2, pp. 202–210, 1968.

66. Dong, Y., C. Su, K. Liu, H. Wang, Z. Zheng, W. Zhao, S. Lu, and A. Lemonidou, “The Catalytic Oxidation of Formaldehyde by FeOx-MnO_2-CeO_2 Catalyst: Effect of Iron Modification”, *Catalysts*, Vol. 11, No. 5, p. 555, 2021.

67. Kolb, G., “Review: Microstructured Reactors for Distributed and Renewable Production of Fuels and Electrical Energy”, *Chemical Engineering and Processing: Process Intensification*, Vol. 65, pp. 1–44, 2013.

68. Koybasi, H. H. and A. K. Avci, “Modeling of a Membrane Integrated Catalytic Microreactor for Efficient DME Production from Syngas with CO_2”, *Catalysis Today*, Vol. 383, pp. 133–145, 2022.

69. Koybasi, H. H. and A. K. Avci, “Numerical Analysis of CO_2-to-DME Conversion in a Membrane Microchannel Reactor”, *Industrial & Engineering Chemistry Research*, Vol. 61, No. 30, pp. 10846–10859, 2022.

70. Bac, S. and A. K. Avci, “Ethylene Oxide Synthesis in a Wall-Coated Microchannel Reactor with Integrated Cooling”, *Chemical Engineering Journal*, Vol. 377, p. 120104, 2019.

71. Wilke, C. R., “A Viscosity Equation for Gas Mixtures”, *The Journal of Chemical Physics*, Vol. 18, No. 4, pp. 517–519, 1950.

72. Bird, R. B., W. E. Stewart, and E. N. Lightfoot, *Transport Phenomena*, Second Edition, Wiley, New York, 2001.

73. Fairbanks, D. F. and C. R. Wilke, “Diffusion Coefficients in Multicomponent Gas Mixtures”, *Industrial & Engineering Chemistry Research*, Vol. 42, No. 3, pp. 471–475, 1950.

74. Fuller, E. N., P. D. Schettler, and J. C. Giddings, "New Method for Prediction of Binary Gas-Phase Diffusion Coefficients", *Industrial & Engineering Chemistry Research*, Vol. 58, No. 5, pp. 18–27, 1966.

75. Kapteijn, F. and J. A. Moulijn, "Laboratory Catalytic Reactors: Aspects of Catalyst Testing", *Handbook of Heterogeneous Catalysis*, pp. 2019–2045, 2008.

76. Rosowski, F., A. Hornung, O. Hinrichsen, D. Herein, M. Muhler, and G. Ertl, "Ruthenium Catalysts for Ammonia Synthesis at High Pressures: Preparation, Characterization, and Power-Law Kinetics", *Applied Catalysis A: General*, Vol. 151, No. 2, pp. 443–460, 1997.